12-2001

Structural Studies of Metastable Nanocrystalline Magnesium Titanate Ceramics

Renmei Xu
Western Michigan University

Recommended Citation

Xu, Renmei, "Structural Studies of Metastable Nanocrystalline Magnesium Titanate Ceramics" (2001). *Masters Theses*. 4779.
https://scholarworks.wmich.edu/masters_theses/4779

STRUCTURAL STUDIES OF METASTABLE NANOCRYSTALLINE MAGNESIUM TITANATE CERAMICS

by

Renmei Xu

A Thesis
Submitted to the
Faculty of The Graduate College
in partial fulfillment of the
requirements for the
Degree of Master of Science
Department of Construction Engineering, Materials
Engineering, and Industrial Design

Western Michigan University
Kalamazoo, Michigan
December 2001

ACKNOWLEDGMENTS

I would like to begin by acknowledging the influence of Dr. Pnina Ari-Gur, my advisor in Western Michigan University. She inspired my interest in nanostructured ceramics two years ago, shared with me her perceptions of this topic, and ultimately led me to the work contained in this thesis.

Secondly, I would like to thank Dr. James W. Richardson, Jr. of Argonne National Laboratory and Dr. Corinna Wauchope of the University of Michigan, who helped me to do the experiments, answered my questions, and spent time to discuss with me. I also thank the members of my graduate committee, Dr. Massood Atashbar and Dr. John B. Miller, for taking the time to review my work and give me helpful advice.

Lastly, I would like to thank my parents and all my friends. Although they couldn't understand what I had done, their support was always there when I needed it. Now I have nothing but this stack of paper to show my gratitude.

Renmei Xu

STRUCTURAL STUDIES OF METASTABLE NANOCRYSTALLINE MAGNESIUM TITANIUM OXIDE

Renmei Xu, M.S.

Western Michigan University, 2001

Nanocrystalline magnesium titanate powders were produced using alkoxides of magnesium and titanium for the sol-gel method. High temperature phases which can only be formed at above 1200°C in equilibrium were formed at much lower temperature 600°C in nanometric system. Cation ordering and structural changes in qandilite (Mg_2TiO_4), geikielite ($MgTiO_3$) and karrooite ($MgTi_2O_5$) were studied by Rietveld refinement of neutron powder diffraction data and X-ray photoelectron spectroscopy. Single qandilite phases were obtained in a wide range of Mg:Ti ratios from 2:038:1 to 1.52:1, and appeared to be $Mg_{2-x}Ti_{1+x}O_4$. Single geikielite phase was obtained with Mg:Ti ratio 1:1.23. Karrooite phases appeared to be $Mg_{1-x}Ti_{2+x}O_5$. The binding energy of nanocrystalline qandilite phase became lower with lower Mg:Ti ratio. The binding energy of nanocrystalline geikielite phase was found similar to the equilibrium phase.

TABLE OF CONTENTS

ACKNOWLEDGMENTS ii

LIST OF TABLES vi

LIST OF FIGURES vii

CHAPTER

I. INTRODUCTION 1

- Properties of Nanostructured Materials 1
- Processing of Nanostructured Ceramic Powders 1
- Importance of Magnesium Titanates 2

II. BACKGROUND 3

- Magnesium Titanate Phases 3
  - $MgO-TiO_2$ Phase Diagram 3
  - Structure of the Three Intermediate Compounds 5
- Nanocrystalline Powder Prepared by Sol-gel Process 8
  - Synthesis Routes of Magnesium Titanates 8
  - Sol-Gel Method for Nanocrystalline Ceramic Oxides 9
- Neutron Powder Diffraction and Rietveld Refinement 10
  - X-ray and Neutron Scattering 10
  - Time-of-flight Neutron Powder Diffraction 12
  - Rietveld Refinement of Neutron Powder Diffraction Data 12
  - Determination of Particle Size 13
- X-ray Photoelectron Spectroscopy 13
  - Principles of the Technique 13
  - Nomenclature Used for the Description of Spectral Features 15

CHAPTER

Collection of the Data 16

III. EXPERIMENTS 17

Materials and Synthetic Procedures 17

Instruments and Analytical Procedures 18

Neutron Powder Diffraction 18

X-ray Photoelectron Spectroscopy 19

IV. RESULTS AND DISCUSSIONS 20

Nonequilibrium Phases 20

Particle Size 21

Structures of Nanocrystalline Phases 23

Single Qandilite Phase 23

Binary Periclase and Qandilite Phases 25

Single Geikielite Phase 26

Binary Geikielite and Karrooite Phases 27

Binary Karrooite and Rutile Phases 31

X-ray Photoelectron Spectroscopy 33

X-ray Photoelectron Spectroscopy Results 33

Oxidation States of Qandilite Phases 34

Oxidation States of Geikielite Phase 35

V. CONCLUSIONS 36

APPENDICES

A. Neutron Powder Diffraction Profiles 37

B. X-ray Photoelectron Spectroscopy Spectra 49

Table of Contents—continued

BIBLIOGRAPHY 54

LIST OF TABLES

1. Crystallization Types of the MgO-TiO$_2$ System above 1500°C 5

2. X-ray and Spectroscopic Notation 15

3. Mg:Ti Atomic Ratios of Samples 17

4. Phases Analysis Results of GPPD Data 20

5. Average Particle Size of the Samples 22

6. Final Rietveld Refinements for Single Qandilite Phase 23

7. Formula Results for Single Qandilite Phase 24

8. Final Rietveld Refinements for Qandilite Phase in Binary Periclase and Qandilite Phases 25

9. Final Rietveld Refinements for Single Geikielite Phase 27

10. Final Rietveld Refinements for Geikielite Phase in Binary Geikielite and Karrooite Phases 28

11. Final Rietveld Refinements for Karrooite Phase in Binary Geikielite and Karrooite Phases 29

12. Formula Results for Binary Geikielite and Karrooite Phases 30

13. Final Rietveld Refinements for Karrooite Phase in Binary Karrooite and Rutile Phases 32

14. Photoelectron Lines in XPS Spectra 33

15. Corrected Photoelectron Lines in XPS Spectra 34

LIST OF FIGURES

1. System MgO-TiO_2 at Atmosphere Pressure in Air 3
2. Analysis of Crystallization Types of Binary MgO-TiO_2 4
3. The Inverse Spinel Structure of Qandilite.. 6
4. Structural of Geikielite, Showing Only the Cation Sublattice....................... 7
5. The Pseudobrookite Structure 8
6. Irregular Variation of Neutron Scattering Amplitude with Atomic Weight Compared with Regular Increase for X-ray Scattering..................... 11
7. The XPS Emission Process for a Model Atom 14
8. Schematic Diagram Showing the Overall Layout of GPPD.......................... 18
9. Relative Phase Amounts of Samples Having Different Compositions.......... 31

CHAPTER I

INTRODUCTION

Properties of Nanostructured Materials

Interest in nanostructured materials has been extremely high over the past two decades. Nanostructured materials have shown considerable physical, mechanical, electromagnetic, optical, and chemical property advantages over their conventional coarse-grained counterparts (Rao & Behera, 1998). In general, a nanostructured material is composed of particles or grains 1 to 100 nm across or of layers or filaments with thickness in that range (Hadjipanyayis & Siegel, 1994). The novel properties arise because pieces of matter less than 100 nm in diameter have properties that are different from conventional solids. Properties of a solid depend fundamentally on the nature of bonding among its constituent atoms and on its microstructures on a variety of length scales. The properties of nanostructured materials and their theoretical basis are still largely unexplored.

Nanostructured materials have many potential applications because of their property advantages. Examples are carbon nanotubes, nanocrystalline semiconductors, nanocrystals, nanoscale devices, nanostructured thin films, and GaAs nanowire crystals, etc. (Rao & Behera, 1998).

Processing of Nanostructured Ceramic Powders

The sol-gel technique has been used to prepare ceramic oxide powder (Zelinski & Uhlmann, 1984). Activity in this area has been increasing at a rapid rate with significant development.

The synthesis of nanocrystalline ceramic oxide powders using sol-gel method has many advantages over other methods. This process involves the use of molecular precursors as starting materials. Since the procedure allows the mixing of precursors at the molecular level, sol-gel method is undoubtedly a low temperature processing technique with a good control over stoichiometry and homogeneity, yielding powders of submicrometer size (Abothu et al., 1999).

Importance of Magnesium Titanates

The magnesium titanates Mg_2TiO_4, $MgTiO_3$, and $MgTi_2O_5$ are important as components in industrial ceramics and natural mineral systems. They have wide applications as dielectric materials for the manufacturing of capacitors because of their useful dielectric properties. They possess a relatively low dielectric constant that varies only slightly with temperature and frequency (Landolt-Bornstein, 1959).

All three magnesium titanates phases synthesized from nanometer precursors, consisting of hydroxides of magnesium and titanium, have improved dielectric properties. They showed a stable dielectric constant over a wide range of frequencies, in contrast with an equivalent commercial powder (Zabicky et al., 1997). Therefore, an understanding of the structural variations observed in these nanostructured compounds and their effects on the stability relations in the system MgO-TiO_2 would be beneficial for estimation of properties on more complex systems with related structures.

CHAPTER II

BACKGROUND

Magnesium Titanate Phases

MgO-TiO$_2$ Phase Diagram

MgO and TiO$_2$ constitute a binary ceramic structure as shown in Figure 1. The phase diagram reveals that Mg$_2$TiO$_4$, MgTiO$_3$, and MgTi$_2$O$_5$ are three intermediate compounds in the MgO-TiO$_2$ system.

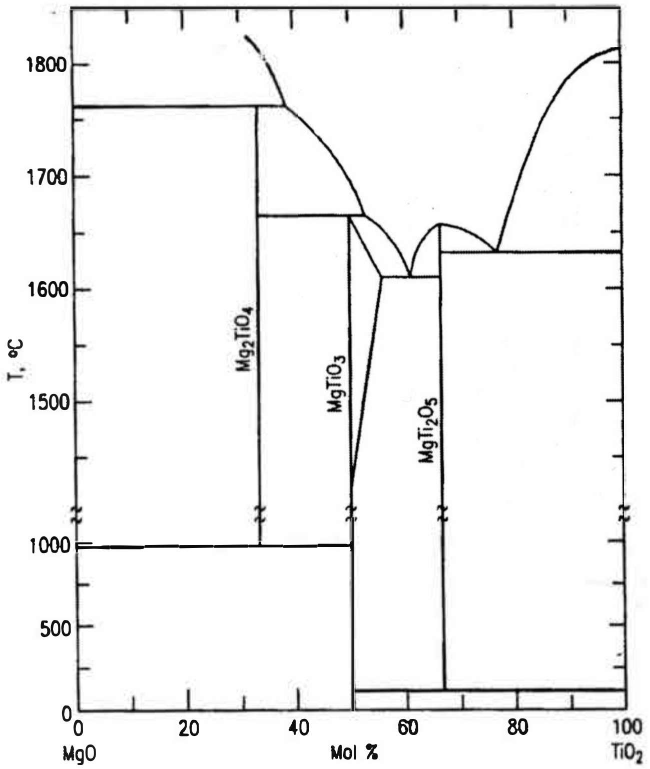

Figure 1. System MgO-TiO$_2$ at Atmosphere Pressure in Air (Wechsler & Navrotsky, 1984).

Mg_2TiO_4, $MgTiO_3$ and $MgTi_2O_5$ are the minerals qandilite, geikielite and karrooite, respectively. Mg_2TiO_4 and $MgTi_2O_5$ are usually found to be stable only at high temperatures because of configurational entropy arising from cation disorder (Wechsler & Navrotsky, 1984).

Crystallization in a binary system can be generally simplified through the division of the diagram into vertical composition bands, each vertical line intersecting a triple point or corresponding a compound composition. The analysis of the crystallization types of the $MgO-TiO_2$ system is shown in Figure 2 and Table 1.

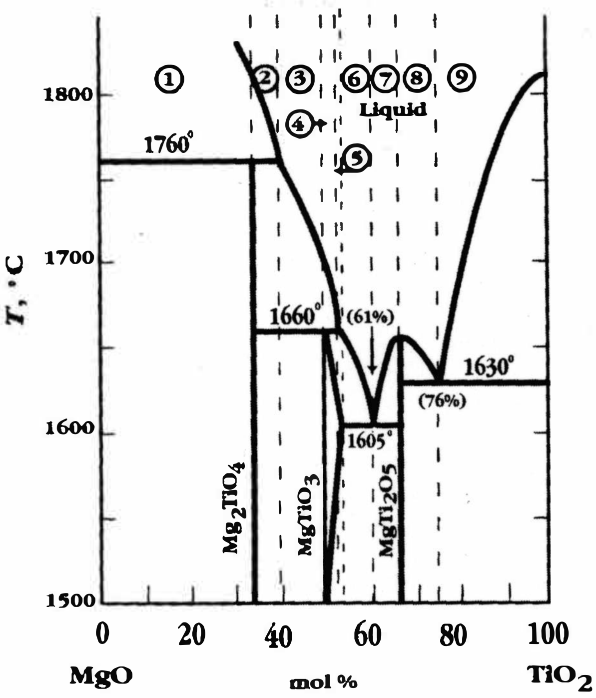

Figure 2. Analysis of Crystallization Types of Binary $MgO-TiO_2$ (McHale, 1998).

Table 1

Crystallization Types of the MgO-TiO_2 System above 1500°C (McHale, 1998)

Region	Range (mol% TiO_2)	Liquidus [°C]	Primary phase	Solidus [°C]	Solid phases
1	0-33	≥1810	MgO	1760	MgO +Mg_2TiO_4
2	33-39	1810-1760	MgO	1660	Mg_2TiO_4 +$MgTiO_3$
3	39-50	1760-1700	Mg_2TiO_4	1660	Mg_2TiO_4 +$MgTiO_3$
4	50-53	1700-1660	Mg_2TiO_4	1660-1620	$MgTiO_3$ss +$MgTi_2O_5$
5	53-54	1660-1650	$MgTiO_3$	1620-1605	$MgTiO_3$ss +$MgTi_2O_5$
6	54-61	1650-1605	$MgTiO_3$	1605	$MgTiO_3$ss +$MgTi_2O_5$
7	61-67	1605-1660	$MgTi_2O_5$	1605	$MgTi_2O_5$ +$MgTiO_3$ss
8	67-76	1660-1630	$MgTi_2O_5$	1630	$MgTi_2O_5$ +TiO_2
9	76-100	1630-1815	TiO_2	1630	$MgTi_2O_5$ +TiO_2

Structure of the Three Intermediate Compounds

Mg_2TiO_4

Mg_2TiO_4 (qandilite) has the inverse spinel ($BABX_4$) structure with space group $fd\bar{3}m$ (Wechsler & Von Dreele, 1989). Spinel (AB_2X_4) structure is characterized by a cubic, close-packed array of O^{2-} spheres with the divalent and trivalent cations distributed in the interstices (Von Hippel, 1954). There are two kinds of interstitial positions in the oxygen lattice, tetrahedral sites enclosed by four oxygen ions and octahedral sites formed by six oxygen ions. Twice as many octahedral as tetrahedral sites are occupied. In the normal spinel structure, the A^{2+} cations occupy one-eighth of the tetrahedral sites and the B^{3+} one-half of the octahedral sites. In the inverse spinel structure, the A^{2+} cations and half the B^{3+} cations occupy octahedral sites while the remaining B^{3+} cations are on tetrahedral sites.

Mg_2TiO_4 can also be written as $MgTiMgO_4$, which means that the Ti^{4+} cations and half the Mg^{2+} cations occupy one-half of the octahedral sites and the remaining half Mg^{2+} cations are on one-eighth of the tetrahedral sites, as shown in Figure 3.

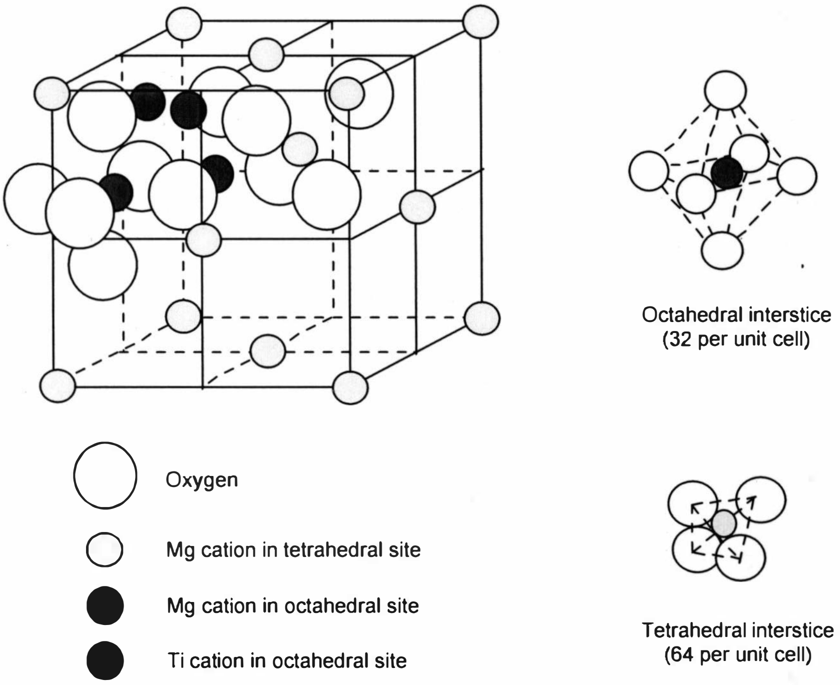

Figure 3. The Inverse Spinel Structure of Qandilite (Von Hippel, 1954).

$MgTiO_3$

$MgTiO_3$ (geikielite) has the ilmenite structure with space group $R\bar{3}$ (Wechsler & Von Dreele, 1989), which involves intermediate-size cations that fit into octahedral interstitial positions to produce an ordered derivative of the corundum (Al_2O_3) structure. In corundum, two thirds of the octahedral sites are filled (Chiang et al., 1997). In $MgTiO_3$, Mg^{2+} and Ti^{4+} substitute Al^{3+} orderly into layers that alternate along the hexagonal *c* direction, which is shown in Figure 4.

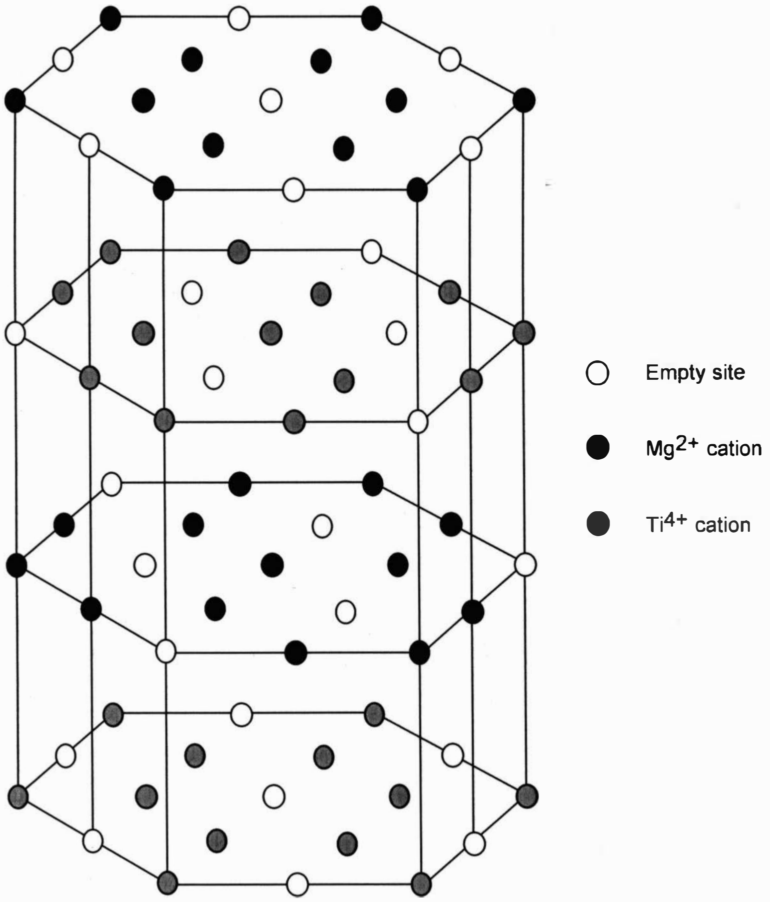

Figure 4. Structure of Geikielite, Showing Only the Cation Sublattice (Chiang et al., 1997).

$MgTi_2O_5$

$MgTi_2O_5$ (karrooite) has the pseudobrookite structure, with space group *Cmcm* (Wechsler & Von Dreele, 1989). The structure consists of bands of edge-sharing octahedra extending in the b direction, as shown in Figure 5. Cations are accommodated in two distinct octahedral sites, four M1 sites (darker ones) and eight

M2 sites (brighter ones). The M1 site is larger and more distorted than M2, and the lattice parameters (*a, b, c*) and volume (*V*) of $MgTi_2O_5$ were found to depend strongly on quench temperature (Wechsler & Navrotsky, 1984).

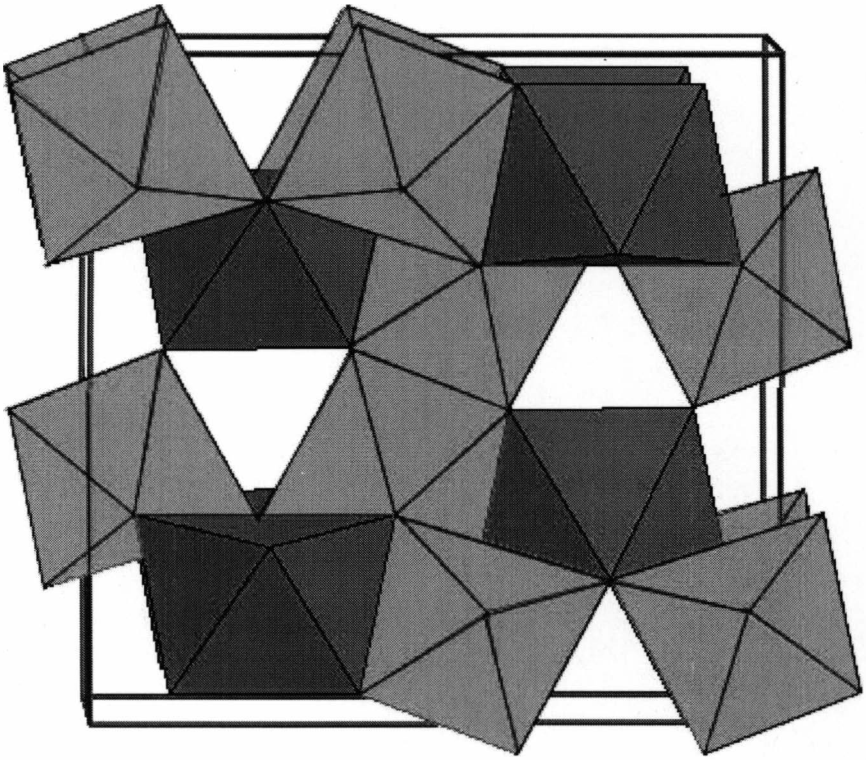

Figure 5. The Pseudobrookite Structure (Smyth, 2001).

Nanocrystalline Powder Prepared by Sol-gel Process

Synthesis Routes of Magnesium Titanates

Syntheses of magnesium titanates are comprised of: solid-state reaction methods (Wechsler & Navrotsky, 1984), coprecipitation (Baura-Pena et al., 1991), thermal decomposition of peroxide precursors (Pfaff, 1994), hydrothermal (Shvets,

1980) and most recently mechanochemical complexation (Liao & Senna, 1995) and nanocomposite and monophasic (Abothu et al., 1999) routes.

The above methods have some disadvantages. For example, conventional solid-state synthesis from oxide precursors requires high temperatures around 1400°C because of the large diffusion distances and it often results in relatively large and varied grain sizes with various impurity contents due to repeated calcination and grinding steps involved. For coprecipitation method, since Mg and Ti hydroxides precipitate at different pH ranges, coprecipitation of these ions as hydroxides requires a very high pH of the order of 10-12 to ensure complete precipitation of Mg (Abothu et al., 1999). In the other hand, the new methods are still under investigation and need to be improved.

Sol-Gel Method for Nanocrystalline Ceramic Oxides

Nanostructured ceramic powders can be produced by the sol-gel method when starting from nanometer precursors. Usually alkoxides are used as starting materials. These compounds have the general formula $M(OR)_n$ where M is a metal ion and R is an alkyl group (C_nH_{2n+1}). With additions of water, the metal alkoxides readily hydrolyze.

The hydrolysis reaction may be represented as (Zelinski & Uhlmann, 1984):

$$M(OR)_n + xH_2O \rightarrow M(OH)_{n-x} + xROH$$

Hydrolysis is followed by condensation to form M--O--M bonds by either of two reactions:

(a) Dehydration:

$--M--OH + HO-M \rightarrow --M--O--M-- + H_2O$

(b) Dealcoholation:

$--M--OH + RO-M \rightarrow --M--O--M-- + ROH$

The gel is then calcinated at a moderate temperature that is sufficiently high to cause conversion of the hydroxide into oxide, but sufficiently low to avoid crystal growth beyond the desired range.

The synthesis of magnesium titanates uses hydroxides of magnesium and titanium as precursors. Reaction of the hydroxides (resulting from the hydrolysis of alkoxides) requires low temperatures about 660°C (Baura-Pena et al., 1991) and 550°C at 100MPa under hydrothermal conditions (Shvets et al., 1980).

Neutron Powder Diffraction and Rietveld Refinement

X-ray and Neutron Scattering

In the case of X-ray scattering, the fundamental scattering bodies are electrons that, by virtue of their charge, interact with the incident X-radiation. Therefore, the amplitude scattered by electrons is proportional to the atomic number (Bacon, 1962). As the angle between the incident and scattered directions increases, this amplitude will fall off quite rapidly because the dimensions of the electronic cloud are comparable with the wavelength of the X-rays. For a given atom the rate of fall depends on $(\sin\theta)/\lambda$, where θ is the Bragg angle and 2θ is the angle of scattering, and is described by the well-known 'atomic scattering factor' or 'form factor' f_X (Bacon, 1962).

In the case of neutron scattering, the fundamental scattering bodies in most atoms are the nucleus and not the electrons. Most atoms scatter neutrons equally well within a factor of two or three, in contrast to the rapid increase with atomic number of the X-ray scattering amplitude, as shown in Figure 6.

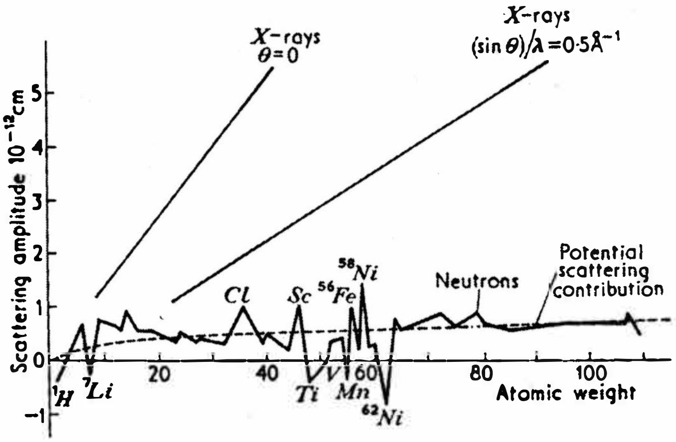

Figure 6. Irregular Variation of Neutron Scattering Amplitude with Atomic Weight Compared with Regular Increase for X-ray Scattering (Bacon, 1954).

Not only does the neutron scattering amplitude show no regular or rapid increase with atomic number but it also shows no variation with the angle θ. The isotropic nature of the scattering is because the dimensions of the nucleus, unlike those of the cloud of electrons, are small in comparison with the typical neutron wavelength of 1Å. Consequently, the 'form factor' for neutron scattering is close to a straight line (the dashed line in Figure 6).

The advantage of neutron diffraction can be used in the MgO-TiO$_2$ system. Ti has negative amplitude for neutron scattering while Mg has a positive one. This makes it possible to distinguish between sites that are occupied by Ti or Mg. Although oxygen is a light element, it has values similar to those of the heavy elements in neutron scattering (Wormald, 1973). This enables more accurate determination of the location of oxygen in the structure by neutron diffraction than by X-ray diffraction.

Time-of-flight Neutron Powder Diffraction

Conventional neutron powder diffractometers utilize a constant-wavelength neutron beam. Later, there has been considerable interest in pulsed neutron sources for time-of-flight (TOF) powder diffractometry (Turberfield, 1970). In the case of TOF diffraction at a reactor resource, a chopper produces a pulsed neutron beam and the diffraction pattern from a sample using this beam is obtained at a time-focused counter array as a function of the neutron TOF (Buras & Holas, 1968). In this way one can observe diffraction patterns to quite small d spacings.

An alternative source that has shown much promise is the proton accelerator or electron LINAC pulsed spallation neutron source. Here the interaction between the proton or electron beam and the heavy-metal target (usually tungsten or uranium) generates high-energy neutrons, which are moderated to epithermal and thermal energies before they are used for diffraction (Von Dreele et al., 1982).

Rietveld Refinement of Neutron Powder Diffraction Data

The technique of 'Rietveld refinement' has been applied very successfully to neutron powder diffraction data (Rietveld, 1969; Cheetham & Taylor, 1978). The Bragg reflections in these patterns have a Gaussian peak shape with a full-width at half-maximum (FWHM) that varies as a function of the diffraction angle θ.

$$(\mathrm{FWHM})^2 = U \tan^2\theta + V \tan\theta + W \tag{1}$$

Typically, the refinement is achieved by minimizing the sum of squares of the weighted differences between the observed and calculated intensities for every point in the profile under the Bragg reflections by adjusting structural parameters (i.e. lattice parameters, atom coordinates and thermal parameters) and profile parameters (i.e. U, V, W and diffractometer zero point) (Von Dreele, et al., 1982).

Determination of Particle Size

The dependence of properties on grain size makes its measurement very important. The grain sizes encountered in commercial metals and alloys range from about 1000 to 1 μm. The term "particle size" is usually used if the size of the individual crystals is less than about 0.1 μm (Cullity, 1990).

The particle size can be determined from the broadening of the diffraction peaks. The particle size (p) is given by

$$p = CK/\gamma_2 \tag{2}$$

where C is the diffractometer constant, K is the Scherrer constant, γ_2 is one of the profile coefficients and the units for p are Å (Larson & Von Dreele, 1985-1994).

X-ray Photoelectron Spectroscopy

Principles of the Technique

Surface analysis by X-ray Photoelectron Spectroscopy (XPS) is accomplished by irradiating a sample with monoenergetic soft X-rays and then analyzing the energy of the detected electrons. Mg Kα (1253.6 eV) or Al Kα (1486.6 eV) X-rays are usually used because these photons have limited penetrating power in a solid on the order of 1-10 micrometers (Moulder et al., 1992). They interact with atoms in the surface region, causing electrons from the outer layers to be emitted by the photoelectric effect. This process is shown in Figure 7.

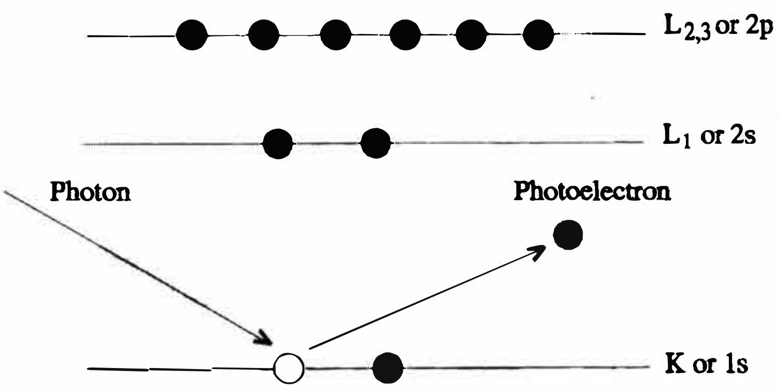

Figure 7. The XPS Emission Process for a Model Atom (Moulder et al., 1992).

The emitted electrons have measured kinetic energies given by:

$$KE = h\nu - BE - \phi \tag{3}$$

where $h\nu$ is the energy of the photon, BE is the binding energy of the atomic orbital from which the electron originates, and ϕ is the work function whose precise value depends on both sample and spectrometer (Briggs & Seah, 1994). Because each element has a unique set of binding energies, XPS can be used to identify and determine the concentration of the elements in the surface. Variations in the elemental binding energies (the chemical shifts) arise from differences in the chemical potential and polarizability of compounds. These chemical shifts can be used to identify the chemical state of the materials being analyzed.

Nomenclature Used for the Description of Spectral Features

The energies of electrons are quantized; that is, electrons are permitted to have only specific values of energy. These allowed electron energies are designated as energy levels or states (Callister, 2000). Every electron in an atom is characterized by quantum numbers. The spectroscopic nomenclature is based on the principal quantum number n and on the electronic quantum numbers l and j. The principal quantum number $n = 1, 2, 3, 4, \ldots$ appears first, then states with quantum number $l = 0, 1, 2, 3, \ldots, n-1$ are designated $s, p, d, f, \ldots$ respectively and follow the first number. Finally the quantum number $j = 1/2, 3/2, 5/2, 7/2, \ldots$ are appended as suffixes (Briggs & Seah, 1994). Table 2 shows the energy levels from $1s_{1/2}$ to $3d_{5/2}$.

Table 2

Spectroscopic Notation

Quantum Numbers			Spectroscopic Level
n	l	j	
1	0	1/2	$1s_{1/2}$
2	0	1/2	$2s_{1/2}$
2	1	1/2	$2p_{1/2}$
2	1	3/2	$2p_{3/2}$
3	0	1/2	$3s_{1/2}$
3	1	1/2	$3p_{1/2}$
3	1	3/2	$3p_{3/2}$
3	2	3/2	$3d_{3/2}$
3	2	5/2	$3d_{5/2}$
	etc.		etc.

Collection of the Data

The electrons emitted by the photoelectric effect are detected by an electron spectrometer according to their kinetic energy. The analyzer is usually operated as an energy window, referred to as the pass energy, accepting only those electrons having energy within the range of the window. To maintain a constant energy resolution, the pass energy is fixed. Incoming electrons having different energy are adjusted to the pass energy before entering the energy analyzer, which is accomplished by applying a variable electrostatic field before the analyzer. The number of electrons for a given detection time and energy is stored and displayed (Moulder et al., 1992). The kinetic energy is then converted to binding energy according to equation (3) for analysis.

CHAPTER III

EXPERIMENT

Materials and Synthetic Procedures

Samples were prepared by Professor J. Zabicky et al. in Ben-Gurion University of the Negev, Israel. The hydroxides of magnesium and titanium of a prescribed ratio were precipitated from toluene by the sol-gel method (Zabicky et al., 1993). To prepare magnesium titanates, the xerogels were heated to 600°C to eliminate solvent residues and the hydroxide groups and to promote the reaction of magnesia and titania to yield magnesium titanates.

The Mg:Ti atomic ratios of the samples obtained from wet analysis are listed in Table 3.

Table 3

Mg:Ti Atomic Ratios of Samples

Sample	Mg:Ti Atomic Ratio	TiO_2 Composition [mol%]
91-74-1	3:1	25.0
91-74-2	2.038:1	32.9
85-68-1	1.852:1	35.1
91-35-1	1.75:1	36.4
91-74-3	1.52:1	39.7
91-75-1	1:1.23	55.2
91-35-2	1:1.503	60.0
91-35-3	1:1.685	62.8
91-75-3	1:1.839	64.8
91-75-4	1:3.31	76.8

Standard $MgTiO_3$ sample (99%, 2 μm powder, from Alfa Co.) was also used to compare with geikielite phase.

Instruments and Analytical Procedures

Neutron Powder Diffraction

Data Collection for Rietveld Refinement

Neutron powder diffraction experiments were performed in Intense Pulsed Neutron Source (IPNS), Argonne National Laboratory. The instrument is IPNS general purpose powder diffractometer (GPPD). The overall layout of GPPD is shown schematically in Figure 8. The target used for the generation of neutron beam is uranium U-238. Multiple detector banks are centered at 2θ values of ±148°, ±90°, ±60°, +30°, and -20°. The resolution $\Delta d/d$ is 2.5×10^{-3} at $2\theta = 148°$.

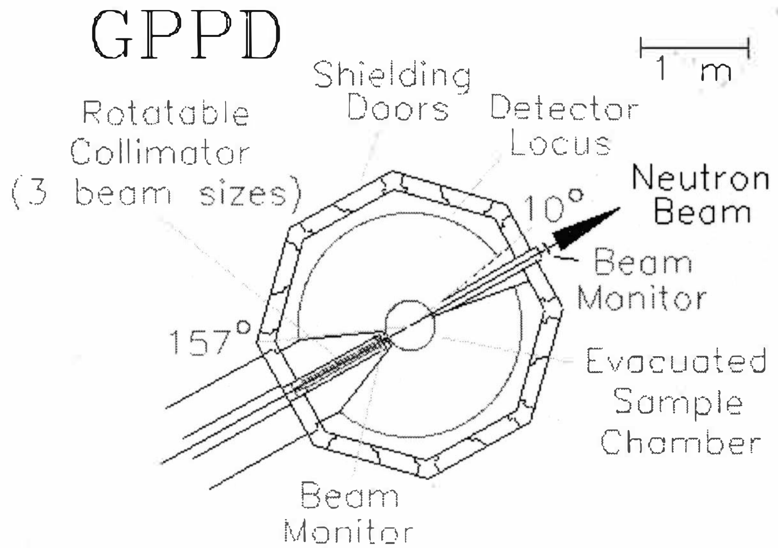

Figure 8. Schematic Diagram Showing the Overall Layout of GPPD (Jorgensen et al., 1989).

Rietveld Refinement of Neutron Powder Diffraction Data

Data were refined using the General Structure Analysis System (GSAS) software (Larson & Von Dreele, 1985-1994). Initial cell and atomic parameters for nanocrystalline qandilite, geikielite, and karrooite phases were taken from Wechsler and Von Dreele (1989).

Determination of Particle Size

The diffractometer constant C was 10385.98. Value of 1 was used for Scherrer constant K (Langford & Wilson, 1978). γ_2 values were obtained from the refinement results of GPPD data.

X-ray Photoelectron Spectroscopy

X-ray Photoelectron Spectroscopy (XPS) experiments were carried out in Electron Microbeam Analysis Laboratory (EMAL), University of Michigan. The XPS model is Perkin Elmer/PHI 5400.

Samples 91-74-2, 91-35-1, 91-74-3, 91-75-1, and standard $MgTiO_3$ (from Alfa) were chosen to perform XPS experiment. Magnesium titanate powder was compressed on an indium foil.

Mg Kα source (1253.6 eV) was used. X-ray photoelectron spectra of In $3d_{5/2}$ and $3d_{3/2}$, Mg $2p$, Ti $2p_{3/2}$ and $2p_{1/2}$, and O $1s$ levels were obtained. The pass energy was 17.9 eV. Work function was arbitrarily set as 4 eV. eV/step was 0.1 eV. Time/step was 200 ms. Sweeps were 3. The pressure was in the low 10^{-8} Torr range.

CHAPTER IV

RESULTS AND DISCUSSIONS

Nonequilibrium Phases

The profiles of GPPD after Rietveld refinement are shown in Appendix A. Observed and calculated profiles are compared to give the difference profile. Phase analysis of GPPD data obtains the results shown in Table 4.

Table 4

Phases Analysis Results of GPPD Data

Sample	Mg:Ti Atomic Ratio	TiO_2 Composition [mol%]	Phases
91-74-1	3:1	25.0	80.7% P + 19.3% Q
91-74-2	2.038:1	32.9	Q
85-68-1	1.852:1	35.1	Q
91-35-1	1.75:1	36.4	Q
91-74-3	1.52:1	39.7	Q
$MgTiO_3$	1:1	50.0	G
91-75-1	1:1.23	55.2	G
91-35-2	1:1.503	60.0	56.3% G + 43.7% K
91-35-3	1:1.685	62.8	50.3% G + 49.7% K
91-75-3	1:1.839	64.8	9.5% G + 90.5% K
91-75-4	1:3.31	76.8	62.3% R + 37.7% K
Note: P – periclase, Q – qandilite, G – geikielite, K – karrooite, R – rutile.			

These results do not comply with the phase diagram shown in Figure 1. High temperature phases like qandilite and karrooite were formed at much lower temperature (600°C). This formation occurs because of the presence of magnesia and titania nanocrystallites in intimate contact, where diffusion processes taking place over a distance of about 20 nm can be accomplished in a relatively short time. The formation of nanometric qandilite, geikielite and karrooïte in nanometric systems can also be ascribed to the significant surface energy reduction taking place in the system (Zabicky et al., 1997).

The nanocrystalline phases differ from the equilibrium structures. At the lower temperature, single-phase products were obtained in a wide range of Mg:Ti ratios. According to equilibrium phase diagram, single qandilite phase can only form when the Mg:Ti ratio equals to 2:1. However, single nanocrystalline qandilite phase was obtained even when Mg:Ti ratio was 1.52:1, which tolerated large deviation from stoichiometry (2:1).

Particle Size

The average particle size results are listed in Table 5. All samples obtained in the nanometric system have particle size within the range of 1 to 100 nm. Qandilite phases showed grain size about 10 nm, and the grain size of geikielite and karrooite phases were in the range of 20 to 80 nm.

Table 5

Average Particle Size of the Samples

Sample	Phase	γ_2	p (nm)
91-74-1	Periclase	30.85	34
	Qandilite	71.99	14
91-74-2	Qandilite	119.35	9
85-68-1	Qandilite	128.55	8
91-35-1	Qandilite	123.11	8
91-74-3	Qandilite	112.32	9
$MgTiO_3$	Geikielite	3.63	286
91-75-1	Geikielite	14.32	72
91-35-2	Geikielite	15.64	66
	Karrooite	31.60	33
91-35-3	Geikielite	13.58	76
	Karrooite	28.61	36
91-75-3	Geikielite	44.24	23
	Karrooite	15.33	68
91-75-4	Karrooite	27.81	37
	Rutile	62.83	16

Structures of Nanocrystalline Phases

Single Qandilite Phase

The parameters from final refinements of samples 91-74-2, 85-68-1, 91-35-1 and 91-74-3, which has Mg:Ti ratio of 2.038:1, 1.852:1, 1.75:1 and 1.52:1 respectively, are given in Table 6. All sites were assumed to be fully occupied.

Single qandilite spinel phase was obtained from all these three samples with TiO_2 compositions up to 39.7%.

Table 6

Final Rietveld Refinements for Single Qandilite Phase

	91-74-2 (2.038:1)	85-68-1 (1.852:1)	91-35-1 (1.75:1)	91-74-3 (1.52:1)
a_0 (Å)	8.42547(4)	8.42708(4)	8.42907(3)	8.43270(2)
V (Å^3)	598.11(3)	598.45(6)	598.88(0)	599.65(3)
Fraction Ti:				
T	0.0325(7)	0.0657(0)	0.0301(6)	0.0
M	0.4127(0)	0.4231(9)	0.4685(3)	0.5460(2)
u (O)	0.2577(2)	0.2581(9)	0.2592(6)	0.2601(3)
U_{iso} T	-0.0084(3)	-0.0082(7)	-0.0087(3)	-0.0064(9)
M	0.0314(0)	0.0279(2)	0.0222(4)	0.0120(2)
U_{11} (O)	0.0087(0)	0.0094(4)	0.0088(5)	0.0097(4)
U_{12} (O)	0.0025(0)	0.0013(7)	0.0013(3)	-0.0007(8)

Note: a_0 = cell parameter; U_{iso} = isotropic temperature factor; U_{11} or U_{12} = anisotropic temperature factor; T = tetrahedral site; M = octahedral site. The U_{iso} values for cations in the same sites were constrained to be equal.

The unit cell parameter a_0 and the oxygen positional parameter u increase when Mg:Ti ratio decreases. The unit cell parameters of these three samples were all smaller than those reported for equilibrium Mg_2TiO_4 (8.44Å) (Wechsler & Von Dreele, 1989).

When TiO_2 composition increases, more titanium atoms occupy the octahedral sites while there are less titanium atoms on the tetrahedral sites. Mg^{2+} cations have larger ionic radius (0.72Å) than Ti^{4+} (0.68Å) cations (Callister, 2000). So more Mg^{2+} on tetrahedral interstices make the unit cell bigger.

The final result of sample 91-74-2 (2.028:1) gives the $Mg_{2.14}Ti_{0.86}O_4$ formula, which agrees to the general formula $Mg_{2-x}Ti_{1+x}O_4$ proposed in the literature for nonstoichiometric cubic qandilite (Cogle et al., 1991). In the same way, formulas for other three samples are obtained and shown in Table 7. These three formulas also agree with general formula $Mg_{2-x}Ti_{1+x}O_4$. With the Mg:Ti ratio decreasing, the x value increases.

Table 7

Formula Results for Single Qandilite Phase

	91-74-2 (2.038:1)	85-68-1 (1.852:1)	91-35-1 (1.75:1)	91-74-3 (1.52:1)
Phase formula	$Mg_{2.14}Ti_{0.86}O_4$	$Mg_{2.09}Ti_{0.91}O_4$	$Mg_{2.03}Ti_{0.97}O_4$	$Mg_{1.91}Ti_{1.09}O_4$
x value	-0.14	-0.09	-0.03	0.09
Mg:Ti ratio	2.49:1	2.30:1	2.09:1	1.75:1

The valences of the ions in these samples are expected to be different from equilibrium phase, which means they have different oxidation states. This will be discussed later following the results of XPS.

The calculated Mg:Ti ratios are all higher than the prescribed ratios of hydroxides of magnesium and titanium prior to the formation of magnesium titanates, and in the same trend. This is under further investigation.

Kimmel and Zabicky (1998) reported a formula $Mg_{1.7}TiO_4$ (based on XRPD), which was derived from the relative occupancy of magnesium cations, 0.85 in tetrahedral sites and 0.85 in octahedral sites. Such formula can be expected from the average ratio of the cations present but not in equilibrium.

Binary Periclase and Qandilite Phases

The parameters from the final refinements of sample 91-74-1 with Mg:Ti ratio of 3:1 are given below for periclase and in Table 8 for qandilite phase.

Periclase has rock salt structure, with space group $fm\bar{3}m$. The final refined parameters are the following: a_0 = 4.21173(9)Å, U_{iso}(Mg) = -0.0006(2), U_{iso}(O) = 0.0110(0).

Table 8

Final Rietveld Refinements for Qandilite Phase in Binary Periclase and Qandilite Phases

	Qandilite
a_0 (Å)	8.42891(9)
V (Å^3)	598.84(7)
Fraction Ti:	
T	0.0
M	0.4763(6)
u (O)	0.2571(9)
U_{iso} T	0.0182(7)
M	-0.0169(7)
U_{11} (O)	0.0084(6)
U_{12} (O)	0.0017(2)

The unit cell parameter a_0 of qandilite phase is close to single qandilite phase in sample 91-35-1 (1.75:1). The u parameter is lower than for those samples with single qandilite phase. Titanium cations only occupy the octahedral sites, which means a completely inverse cation distribution. The formula obtained from the refinement is $Mg_{2.05}Ti_{0.95}O_4$.

The refined phase composition is 80.7% periclase and 19.3% qandilite. So the formula derived from the refinement is 80.7% MgO + 19.3% $Mg_{2.05}Ti_{0.95}O_4$. However, the calculated total Mg:Ti ratio is 6.56:1, which is a lot different from the theoretical Mg:Ti ratio 3:1.

Single Geikielite Phase

The parameters from the final refinements of standard (micro) $MgTiO_3$ and 91-75-1 samples, which has Mg:Ti ratio of 1:1 and 1:1.23 respectively, are given in Table 9. Unlike the refinement of qandilite phases, the occupancy on each site was refined here. Single geikielite phase was obtained from these two samples with TiO_4 compositions up to 55.2%.

The cation positions are not fully occupied in sample 91-75-1 (1:1.23), so the distances between Mg^{2+} and Ti^{4+} layers become smaller, which may be the reason that the unit cell parameter a_0 and c_0 of sample 91-75-1 (1:1.23) are a little smaller than those of standard $MgTiO_3$ sample are.

The formula derived from the refined results of standard $MgTiO_3$ sample is $MgTi_{0.97}O_{2.99}$, which is very close to the theoretical formula $MgTiO_3$. The formula derived from the refined results of sample 91-75-1 (1:1.23) is $MgTi_{0.90}O_{3.43}$, while the theoretical formula for 1:1.23 Mg:Ti ratio is $MgTi_{1.23}O_{3.46}$. The calculated Mg:Ti ratio is higher than the theoretical one herein, which is the same as the results discussed for nanocrystalline qandilite phases.

Table 9

Final Rietveld Refinements for Single Geikielite Phase

	$MgTiO_3$ (1:1)	91-75-1 (1:1.23)
a_0 (Å)	5.05651(7)	5.05231(3)
c_0 (Å)	13.90189(0)	13.89970(0)
V (Å^3)	307.82(8)	307.26(7)
z (Mg)	0.3557(9)	0.3554(9)
z (Ti)	0.1448(4)	0.1456(5)
x (O)	0.3161(2)	0.3153(9)
y (O)	0.0207(8)	0.0193(5)
z (O)	0.2467(4)	0.2473(0)
Fraction (Mg)	1.0000(0)	0.8759(0)
Fraction (Ti)	0.9721(0)	0.7907(4)
Fraction (O)	0.9952(3)	1.0000(0)
U_{iso} (Mg)	0.0034(3)	0.0030(7)
U_{iso} (Ti)	0.0002(0)	-0.0021(2)
U_{11} (O)	0.0026(2)	0.0025(9)
U_{22} (O)	0.0021(9)	0.0027(8)
U_{33} (O)	0.0028(8)	0.0050(3)
U_{12} (O)	0.0012(3)	0.0013(3)
U_{13} (O)	0.0000(4)	-0.0000(1)
U_{23} (O)	0.0009(9)	0.0004(6)

The valences of the ions in 91-75-1 sample are expected to be different from equilibrium $MgTiO_3$ sample, which means they have different oxidation states. This will be discussed later following the results of XPS.

Binary Geikielite and Karrooite Phases

The refined parameters from the final refinements of samples 91-35-2, 91-35-3 and 91-75-3, which has Mg:Ti ratio of 1:1.503, 1:1.685 and 1:1.839 respectively, are given in Table 10 for Geikielite phase and Table 11 for Karrooite phase. The occupancy on each site was refined for geikielite phase, while the positions were assumed to be fully occupied in karrooite phase.

Table 10

Final Rietveld Refinements for Geikielite Phase in Binary Geikielite and Karrooite Phases

	91-35-2 (1:1.503)	91-35-3 (1:1.685)	91-75-3 (1:1.839)
a_0 (Å)	5.05330(1)	5.05313(7)	5.05167(7)
c_0 (Å)	13.89463(0)	13.89616(0)	13.90403(0)
V (Å^3)	307.26(7)	307.28(9)	307.28(6)
z (Mg)	0.3556(4)	0.3556(4)	0.3539(1)
z (Ti)	0.1459(1)	0.1459(8)	0.1499(4)
x (O)	0.3162(8)	0.3159(2)	0.3282(3)
y (O)	0.0190(0)	0.0197(2)	0.0296(0)
z (O)	0.2478(5)	0.2473(9)	0.2465(0)
Fraction (Mg)	0.8303(4)	0.8605(9)	1.0000(0)
Fraction (Ti)	0.7360(5)	0.7947(0)	1.0000(0)
U_{iso} (Mg)	0.0028(6)	0.0034(8)	0.0079(0)
U_{iso} (Ti)	-0.0030(3)	-0.0014(9)	-0.0026(1)
U_{11} (O)	0.0023(8)	0.0027(6)	0.0054(1)
U_{22} (O)	0.0032(1)	0.0035(6)	-0.0030(3)
U_{33} (O)	0.0057(1)	0.0058(6)	-0.0017(7)
U_{12} (O)	0.0017(2)	0.0020(7)	-0.0043(7)
U_{13} (O)	0.0010(8)	0.0008(7)	-0.0005(9)
U_{23} (O)	0.0015(6)	0.0014(0)	-0.0030(7)

Table 11

Final Rietveld Refinements for Karrooite Phase in Binary Geikielite and Karrooite Phases

	91-35-2 (1:1.503)	91-35-3 (1:1.685)	91-75-3 (1:1.839)
a_0 (Å)	3.75333(3)	3.75371(4)	3.74513(6)
b_0 (Å)	9.74685(8)	9.74444(8)	9.74076(0)
c_0 (Å)	9.94553(4)	9.94005(4)	9.96935(5)
V (Å^3)	363.83(9)	363.58(6)	363.68(7)
y (M1)	0.1863(6)	0.1842(2)	0.1935(8)
y (M2)	0.1339(0)	0.1349(6)	0.1337(4)
z (M2)	0.5561(6)	0.5560(8)	0.5601(8)
y (O1)	0.7594(3)	0.7505(6)	0.7645(6)
y (O2)	0.0498(4)	0.0510(3)	0.0461(2)
z (O2)	0.1071(4)	0.1049(0)	0.1163(0)
y (O3)	0.3090(0)	0.3089(6)	0.3116(3)
z (O3)	0.0796(2)	0.0851(3)	0.0709(7)
Fraction Ti: M1	0.5105(5)	0.5058(7)	0.5016(0)
M2	0.7617(4)	0.7661(2)	0.7467(3)
U_{iso} (M1)	0.0092(6)	0.0112(0)	-0.0030(6)
U_{iso} (M2)	-0.0020(5)	0.0014(0)	-0.0020(4)
U_{11} (O1)	0.0032(9)	0.0034(1)	0.0122(7)
U_{22} (O1)	0.0166(8)	0.0661(1)	0.0095(8)
U_{33} (O1)	0.0091(1)	0.0157(9)	0.0144(0)
U_{11} (O2)	0.0004(3)	-0.0008(4)	0.0110(8)
U_{22} (O2)	0.0137(0)	0.0135(0)	0.0074(7)
U_{33} (O2)	0.1417(9)	0.2392(3)	0.0099(1)
U_{23} (O2)	-0.0560(3)	-0.0743(6)	-0.0033(7)
U_{11} (O3)	0.0161(4)	0.0204(6)	0.0028(5)
U_{22} (O3)	0.0270(0)	0.0252(8)	0.0136(1)
U_{33} (O3)	0.0240(7)	0.0419(7)	0.0077(8)
U_{23} (O3)	-0.0025(9)	-0.0088(4)	0.0033(0)

The unit cell parameters of geikielite and karrooite phases in these three samples vary a little, but their volumes are very close.

The formula results are listed in Table 12. The Mg:Ti ratios in geikielite phases are 1.13:1, 1.08:1, and 1:1 respectively, with the total Mg:Ti ratios of the samples decreasing. The formulas of karrooite phases in these three samples agree to the general formula $Mg_{1-x}Ti_{2+x}O_5$ with different x values 0.034, 0.038, and –0.005. These values are very close to zero, in which case it is the equilibrium phase $MgTi_2O_5$.

Table 12

Formula Results for Binary Geikielite and Karrooite Phases

		91-35-2 (1:1.503)	91-35-3 (1:1.685)	91-75-3 (1:1.839)
Geikielite	Formula	$Mg_{0.830}Ti_{0.736}O_3$	$Mg_{0.861}Ti_{0.795}O_3$	$MgTiO_3$
	Mg:Ti ratio	1.13:1	1.08:1	1:1
Karrooite	Formula	$Mg_{0.966}Ti_{2.034}O_5$	$Mg_{0.962}Ti_{2.038}O_5$	$Mg_{1.005}Ti_{1.995}O_5$
	x value	0.034	0.038	-0.005
Total Mg:Ti ratio		1:1.47	1:1.55	1:1.89

The relationship between the phase fractions of geikielite and karrooite phases and the composition of TiO_2 is shown in Figure 9. This result agrees with the phase diagram in Figure 1, but at lower temperature. Combined with the results obtained from the analysis of qandilite phases, it can be concluded that in a nanometric system, the phase transition temperatures are significantly lowered. The diffusion processes can be accomplished in a relatively short time. It can also be ascribed to the significant surface energy reduction (Zabicky et al., 1997).

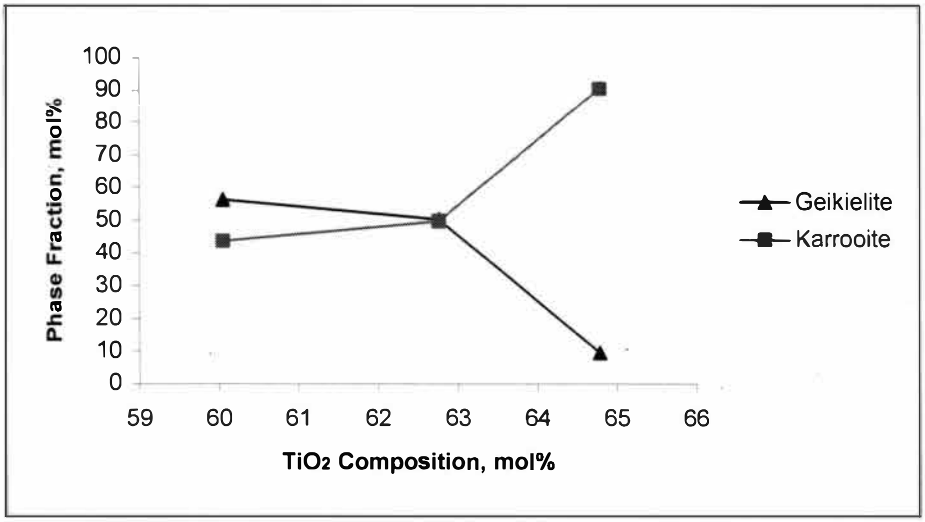

Figure 9. Relative Phase Amounts of Samples Having Different Compositions.

Binary Karrooite and Rutile Phases

The refined parameters from the final refinements of sample 91-75-4 with Mg:Ti ratio of 1:3.31 are given below for rutile and in Table 13 for karrooite phase.

TiO_2 has rutile structure, with space group *P4₂/mnm*. The final refined parameters are the following: a_0 = 4.59697(5)Å, c_0 = 2.95665(1)Å, x(O) = 0.2968(9), U_{iso}(Ti) = 0.0010(9), U_{11}(O) = 0.0075(0), U_{33}(O) = 0.0136(3), U_{12}(O) = -0.0114(6), U_{13}(O) = 0.0000(0).

The unit cell parameters of karrooite phase are different from those of any other samples. Its a_0 and b_0 are smaller while c_0 is larger. Nevertheless, its volume is almost the same. The formula of karrooite phase derived from the final refinement is $Mg_{0.941}Ti_{2.059}O_5$ in this sample, so the x value is 0.059, which is larger than those of other samples.

Table 13

Final Rietveld Refinements for Karrooite Phase in Binary Karrooite and Rutile Phases

a_0 (Å)	3.74363(9)
b_0 (Å)	9.71806(0)
c_0 (Å)	9.98931(4)
V (Å^3)	363.42(0)
y (M1)	0.1965(8)
y (M2)	0.1324(3)
z (M2)	0.5670(2)
y (O1)	0.7710(2)
y (O2)	0.0457(5)
z (O2)	0.1161(4)
y (O3)	0.3128(3)
z (O3)	0.0694(5)
Fraction Ti: M1	0.3532(1)
M2	0.8529(4)
U_{iso} (M1)	0.0084(3)
U_{iso} (M2)	-0.0004(4)
U_{11} (O1)	0.0059(8)
U_{22} (O1)	0.0070(1)
U_{33} (O1)	0.0130(0)
U_{11} (O2)	0.0041(2)
U_{22} (O2)	0.0084(4)
U_{33} (O2)	0.0209(0)
U_{23} (O2)	-0.0026(1)
U_{11} (O3)	0.0017(5)
U_{22} (O3)	0.0133(8)
U_{33} (O3)	0.0039(4)
U_{23} (O3)	0.0055(2)

The refined phase composition is 37.7% karrooite and 62.3% rutile. So the formula is 37.7% $Mg_{0.941}Ti_{2.059}O_5$ + 62.3% TiO_2. The calculated total Mg:Ti ratio is 1:3.94, which is lower than the theoretical Mg:Ti ratio 1:3.31.

X-ray Photoelectron Spectroscopy

X-ray Photoelectron Spectroscopy Results

The raw X-ray photoelectron spectra of In $3d_{5/2}$ and $3d_{3/2}$, Mg $2p$, Ti $2p_{3/2}$ and $2p_{1/2}$, and O $1s$ levels in 91-74-2, 91-35-1, 91-74-3, standard $MgTiO_3$, and 91-75-1 samples are shown in Appendix B, Figure B-1 to B-4. The positions of photoelectron lines obtained from curve fitting are listed in Table 14. Small peaks, which had less than 5% areas, were ignored considering the noise effect.

Table 14

Photoelectron Lines in XPS Spectra

	Line Positions (eV)				
	91-74-2 (2.038:1)	91-35-1 (1.75:1)	91-74-3 (1.52:1)	$MgTiO_3$ (1:1)	91-75-1 (1:1.23)
In $3d_{5/2}$	444.51	444.29	444.63	444.39	444.36
In $3d_{3/2}$	452.06	452.07	452.24	451.92	451.98
Mg $2p$	50.33	50.23	50.55	50.84	50.45
Ti $2p_{3/2}$	460.27	460.27	460.58	460.43	459.94
Ti $2p_{1/2}$	465.83	465.75	466.02	465.92	465.42
O $1s$	531.51 (67.6%) 533.40 (32.4%)	531.36 (57.0%) 532.86 (43.0%)	532.08	531.90	531.61

The In $3d_{5/2}$ levels were used as internal references. After taking the binding energy of In $3d_{5/2}$ for standard $MgTiO_3$ as reference, the corrected line positions are shown in Table 15.

Table 15

Corrected Photoelectron Lines in XPS Spectra

	Line Positions (eV)				
	91-74-2 (2.038:1)	91-35-1 (1.75:1)	91-74-3 (1.52:1)	$MgTiO_3$ (1:1)	91-75-1 (1:1.23)
Mg 2*p*	50.21	50.33	50.31	50.84	50.48
Ti $2p_{3/2}$	460.15	460.37	460.34	460.43	459.97
Ti $2p_{1/2}$	465.71	465.85	465.78	465.92	465.45
O 1*s*	531.39 (67.6%) 533.28 (32.4%)	531.46 (57.0%) 532.96 (43.0%)	531.84	531.90	531.64

Oxidation States of Qandilite Phases

Standard $MgTiO_3$ sample is stoichiometric phase. The formal charges of Mg, Ti, and O ions should be +2, +4, and –2 respectively.

The binding energies of Mg 2*p* obtained in three qandilite samples are about 0.5 – 0.6 eV lower than the value in standard $MgTiO_3$ sample, which means that Mg has lower oxidation state and then the actual charges of Mg are less than +2. Comparing the binding energies of Ti $2p_{3/2}$ and $2p_{1/2}$, the binding energies in qandilite samples are slightly lower, which means the actual charge of Ti are smaller than +4.

The peaks of O 1*s* spectrum are not symmetric in sample 91-74-2 (2.038:1) and 91-35-1 (1.75:1), where two position lines were observed. This means two different oxidation states are present. The reason may be that a small part of tetrahedral sites were partially occupied by titanium cations, which resulted the oxidation status in these sites to be different from others occupied by magnesium cations. However, more oxygen ions have lower binding energies by about 0.5 eV in these two samples. In sample 91-74-3 (1.53:1), the binding energy of O 1*s* is almost the same, which means the oxidation state is in equilibrium.

The above results comply with charge balance. These three qandilite samples are all titanium rich phases having formula $Mg_{2-x}Ti_{1+x}O_4$ with X>0. If they were in stoichiometry, the total charge would be higher than +8. So Mg and Ti cations shift to lower oxidation states, which result in lower positive charge. In the meantime, oxygen ions also shift to lower oxidation states, in the other word, more reduction states, in order to obtain total negative charge more than –8 to balance the positive charge.

Oxidation States of Geikielite Phase

The binding energies in sample 91-75-1 (1:1.23) are lower than in the standard $MgTiO_3$ sample by less than about 0.4 – 0.5 eV. The analysis for qandilite phases can also applied to geikielite phase because it is also titanium rich phase. Therefore, Mg and Ti cations shift to less oxidation states to lower the total positive charge while oxygen anions shift to more reduced state to increase total negative charge until the positive and negative charges are balanced.

CHAPTER V

CONCLUSIONS

Nanocrystalline magnesium titanates powder with a particle size within the range of 1 – 100 nm were formed at much lower temperature (600°C) in nanometric system. Qandilite phases showed much smaller grain sizes about 10 nm than geikielite and karrooite phases from 20 to 80 nm.

Single qandilite phases were obtained in a wide range of Mg:Ti ratios from 2:038:1 to 1.52:1, and appeared to be $Mg_{2-x}Ti_{1+x}O_4$. Only the sample with 1.52:1 Mg:Ti ratio has a completely inverse cation distribution. , Mg and Ti are disordered in both octahedral site and tetrahedral site in other samples with Mg:Ti ratio of 2.038:1, 1.75:1 and 1.52:1. Oxidation states of Mg, Ti and oxygen ions are all lowered, but by different degree, to keep the charge balanced.

Single geikielite phase was obtained with Mg:Ti ratio 1:1.23. Mg and Ti are completely ordered between two octahedral sites. The oxidation states of Mg, Ti and Oxygen ions are lower than stoichiometric geikielite phase by about 0.4 – 0.5 eV.

In the binary geikielite and karrooite system, the phase amount of geikielite decreased while karrooite increased with Mg:Ti ratio decreasing. Geikielite phases approached stoichiometric state with Ti:Mg ratio increasing. Karrooite phases appeared to be $Mg_{1-x}Ti_{2+x}O_5$ with small x values and Mg-Ti distribution is disordered in all samples.

Appendix A

Neutron Powder Diffraction Profiles

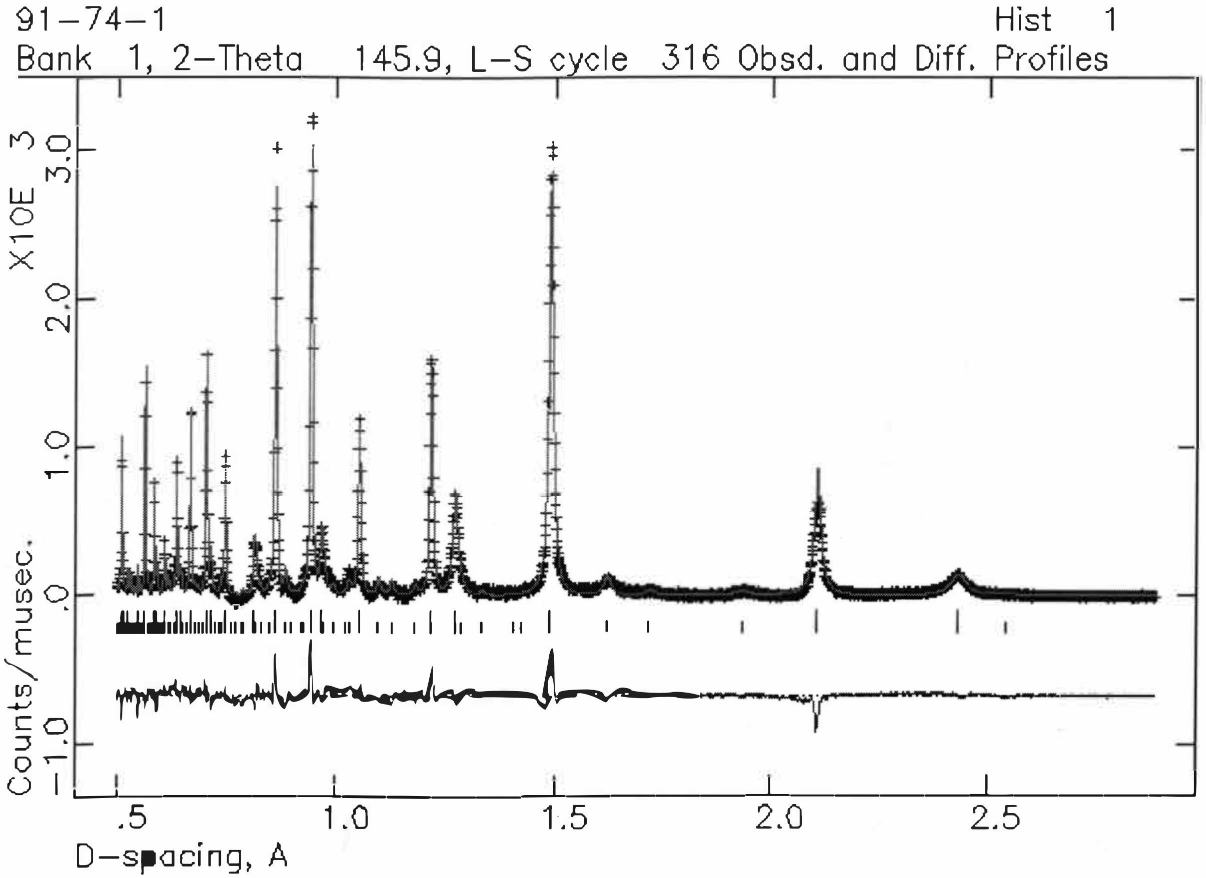

Figure A-1. Neutron Powder Diffraction Profiles of Sample 91-74-1.

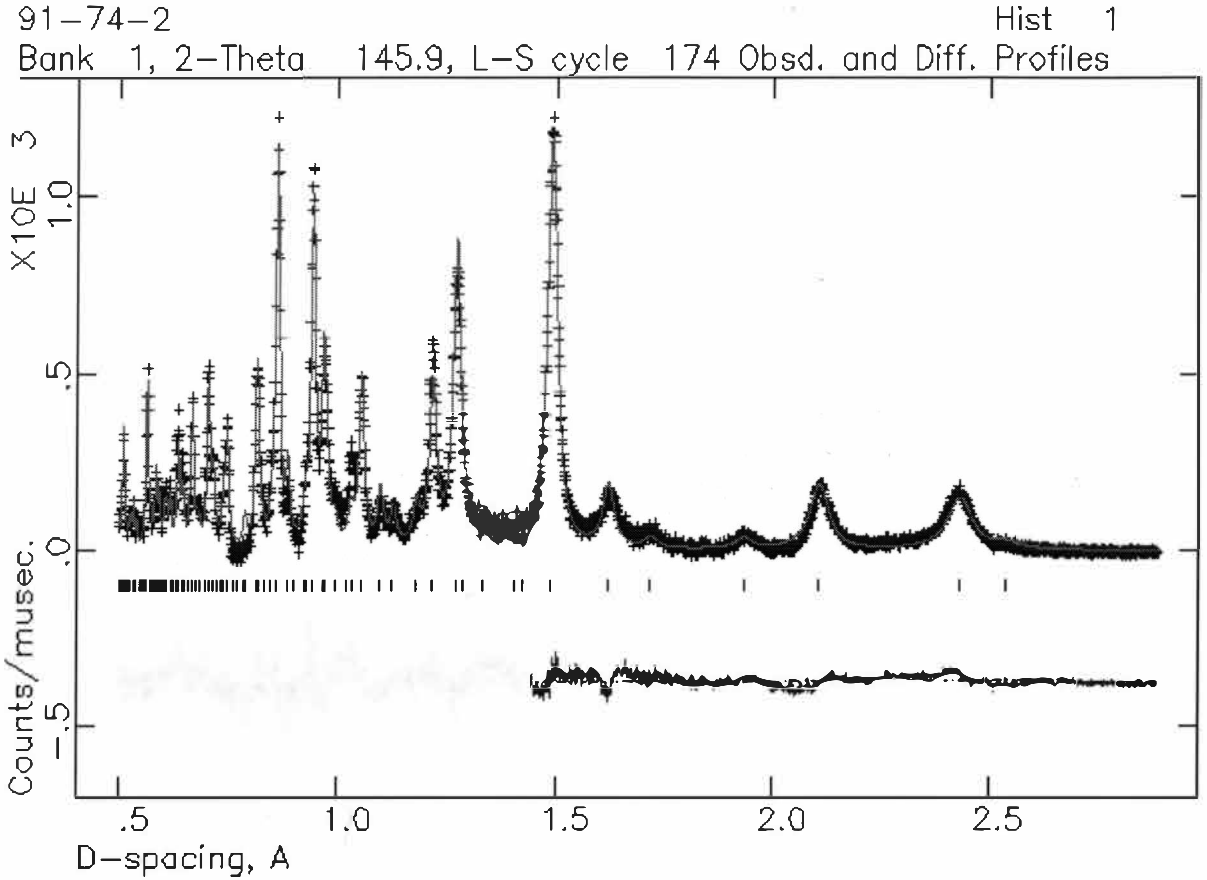

Figure A-2. Neutron Powder Diffraction Profiles of Sample 91-74-2.

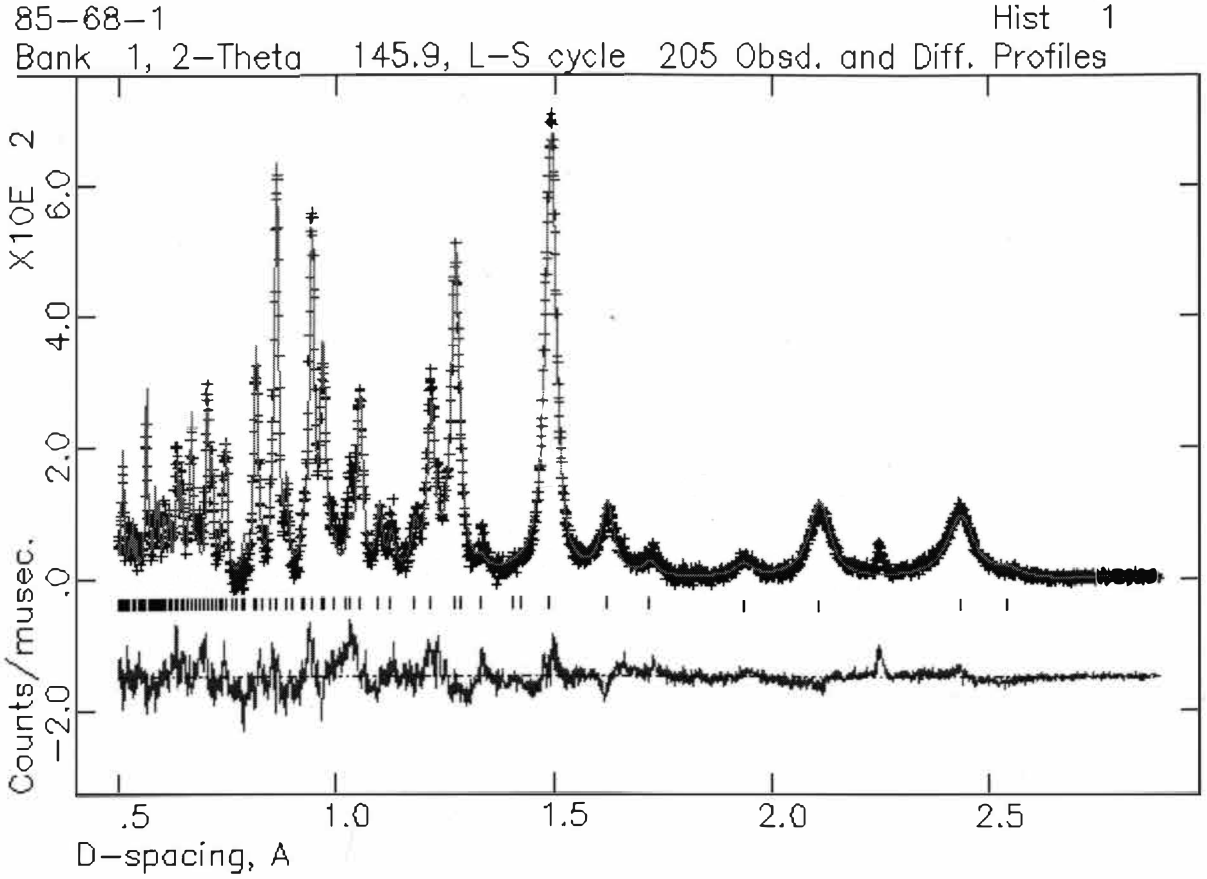

Figure A-3. Neutron Powder Diffraction Profiles of Sample 85-68-1.

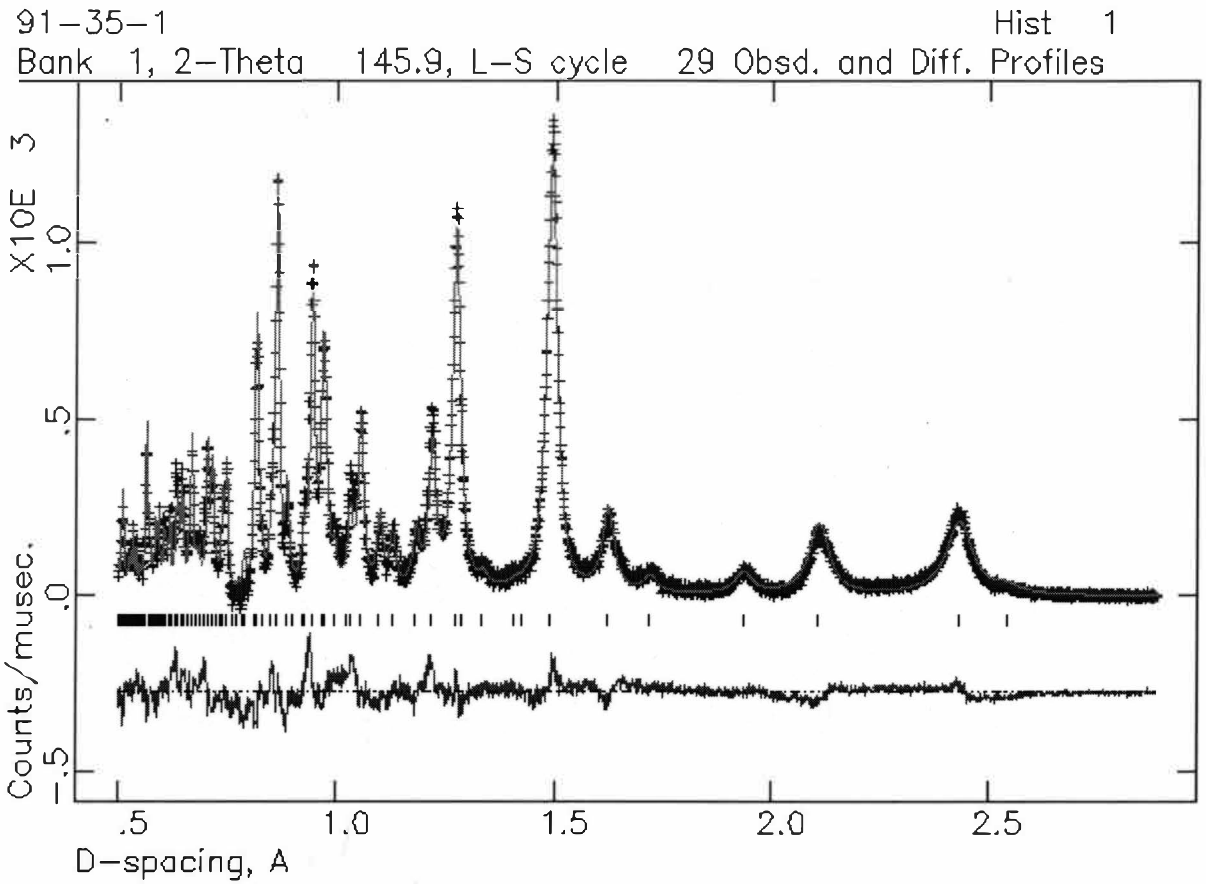

Figure A-4. Neutron Powder Diffraction Profiles of Sample 91-35-1.

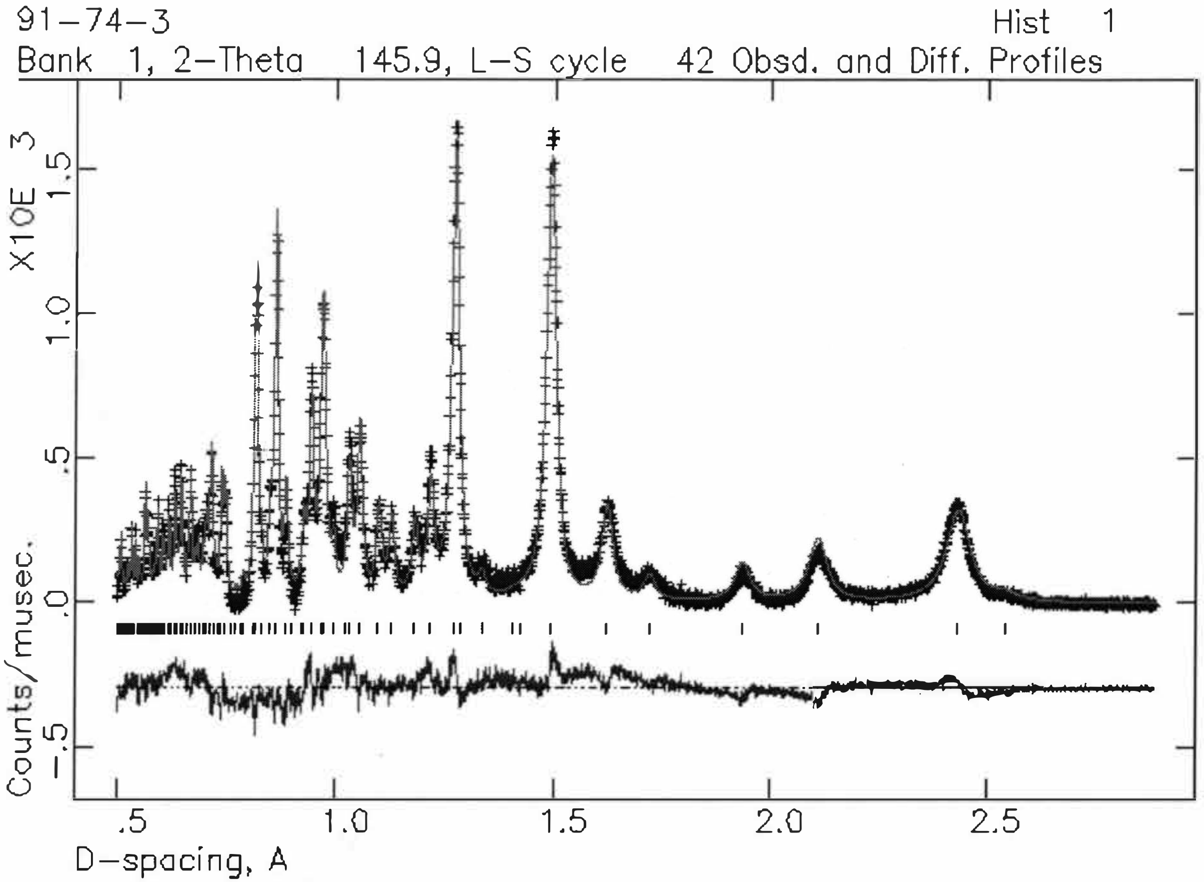

Figure A-5. Neutron Powder Diffraction Profiles of Sample 91-74-3.

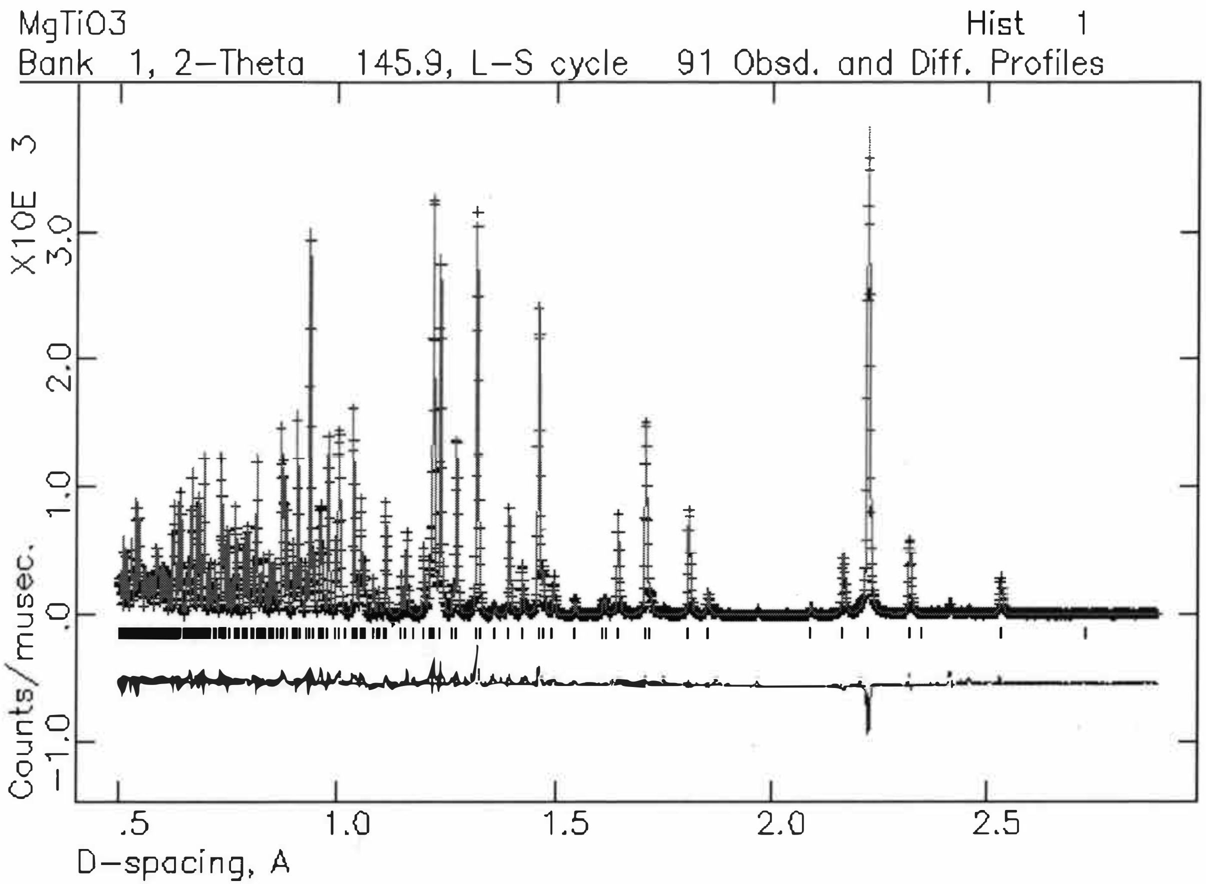

Figure A-6. Neutron Powder Diffraction Profiles of Sample $MgTiO_3$.

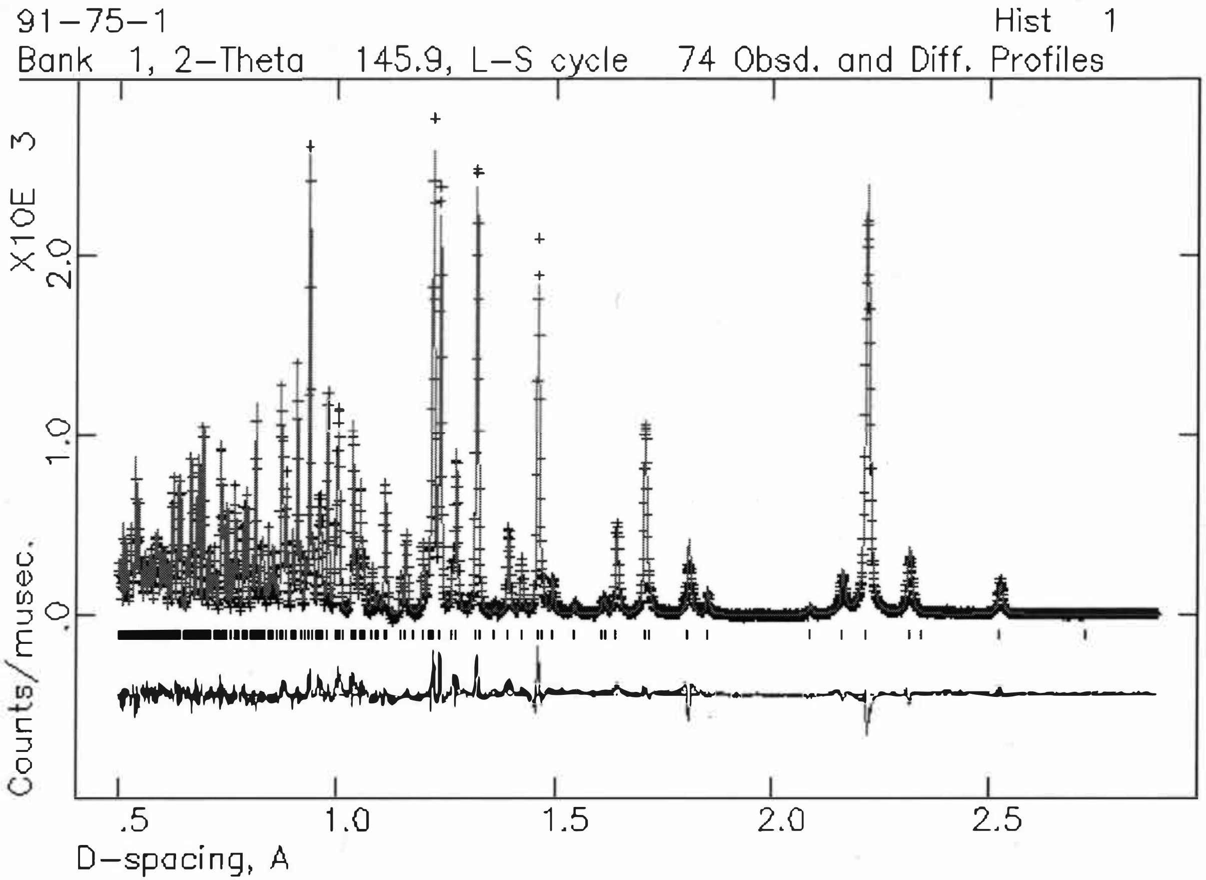

Figure A-8. Neutron Powder Diffraction Profiles of Sample 91-75-1.

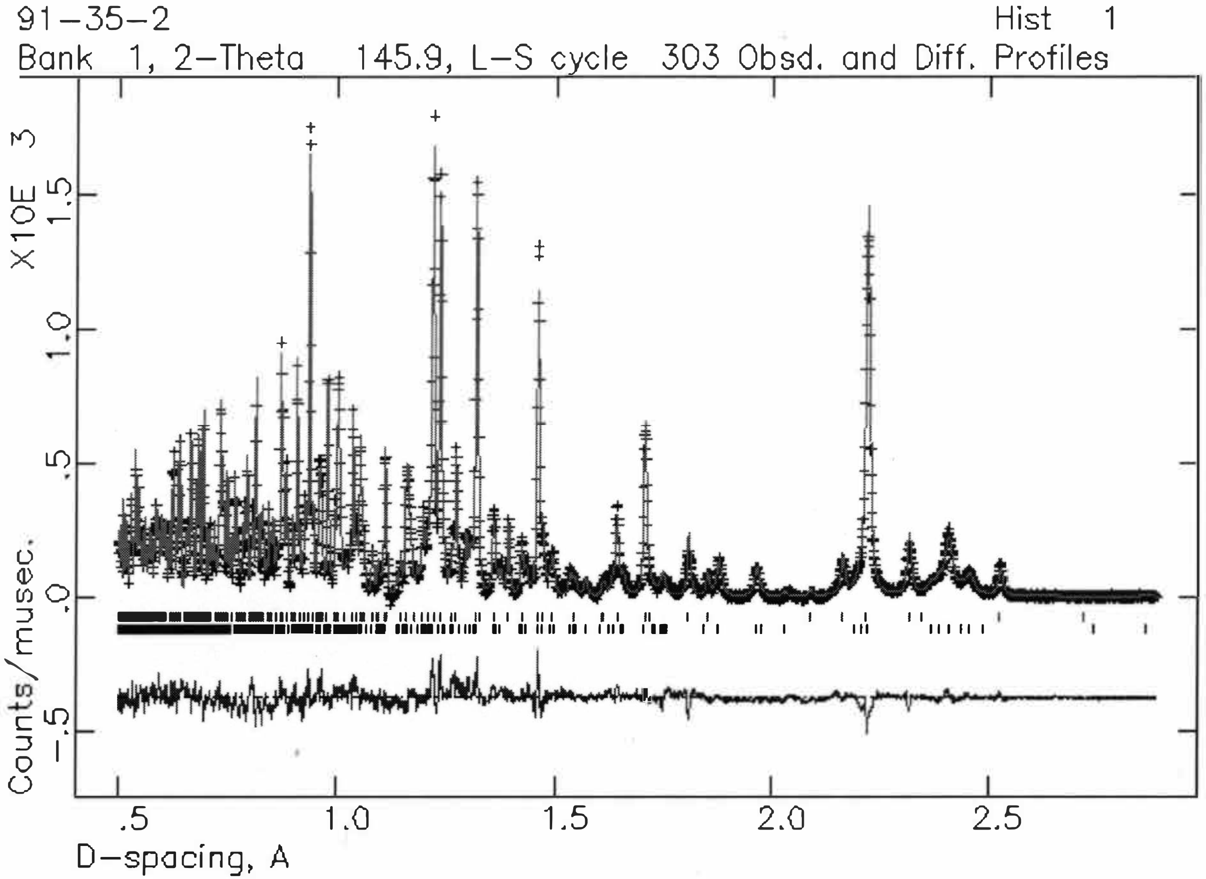

Figure A-9. Neutron Powder Diffraction Profiles of Sample 91-35-2.

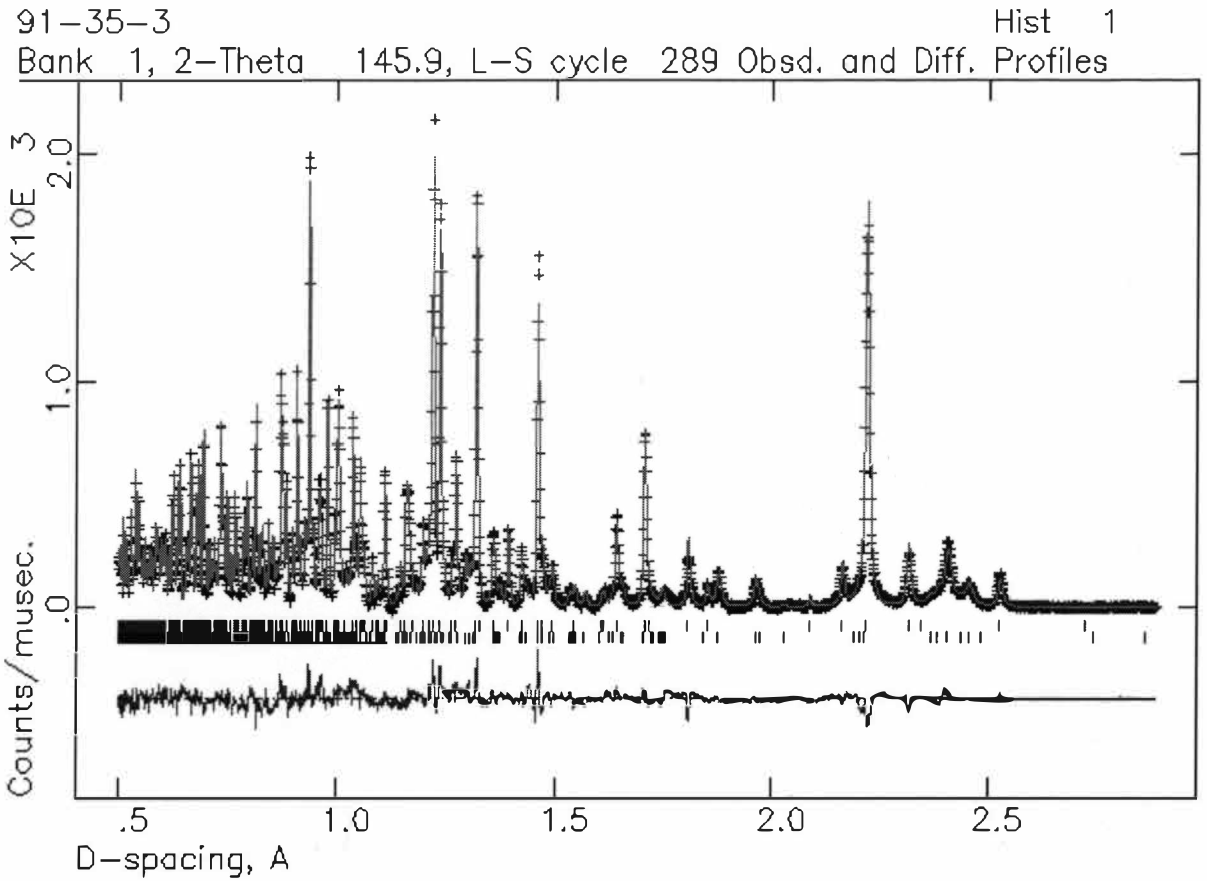

Figure A-10. Neutron Powder Diffraction Profiles of Sample 91-35-3.

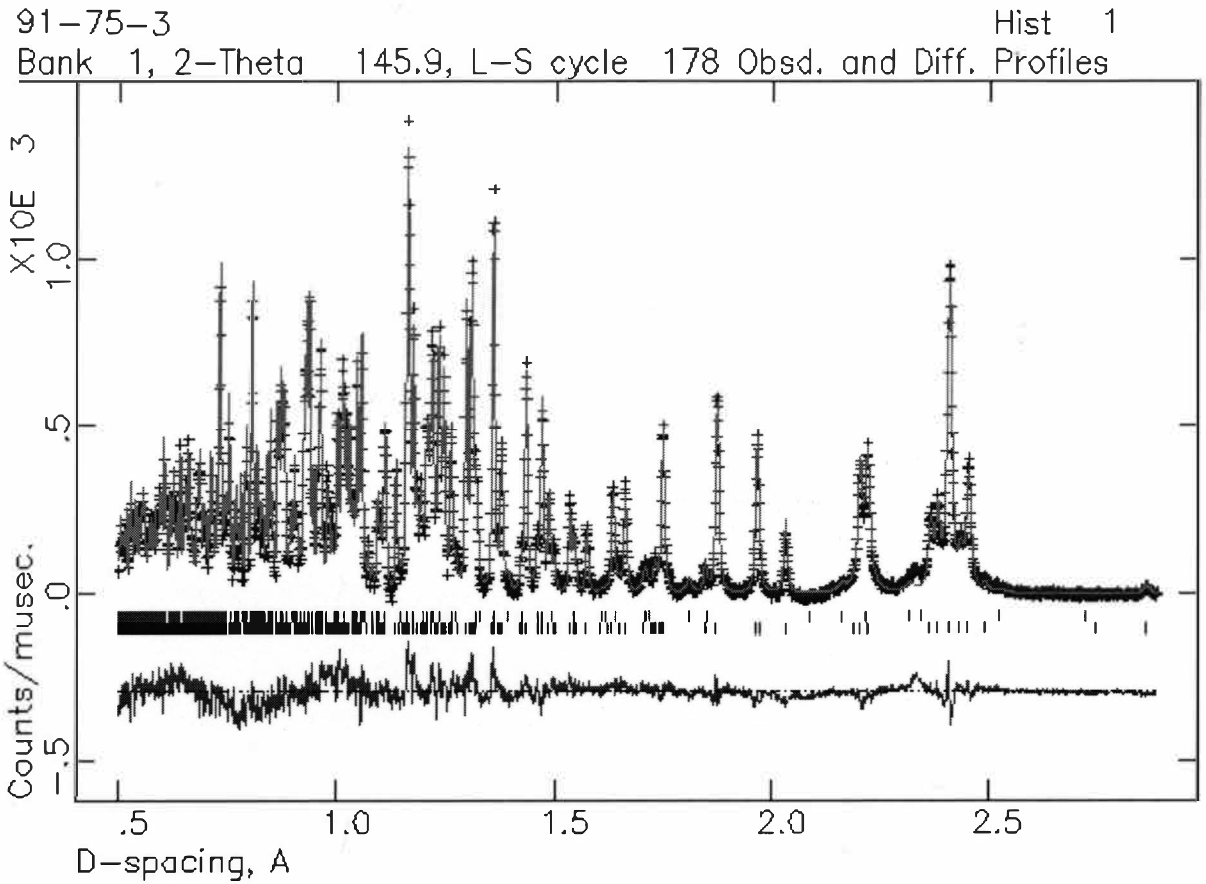

Figure A-11. Neutron Powder Diffraction Profiles of Sample 91-75-3.

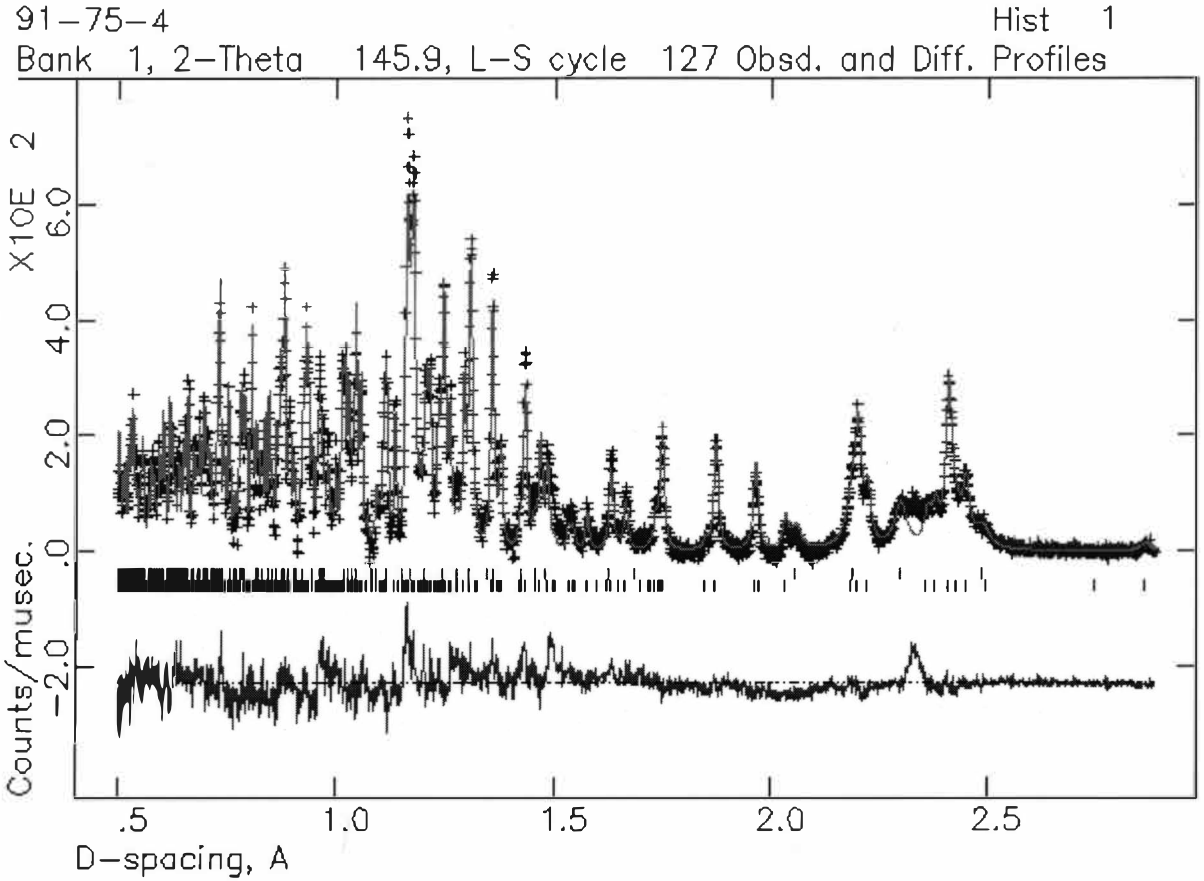

Figure A-12. Neutron Powder Diffraction Profiles of Sample 91-75-4.

Appendix B

X-ray Photoelectron Spectroscopy Spectra

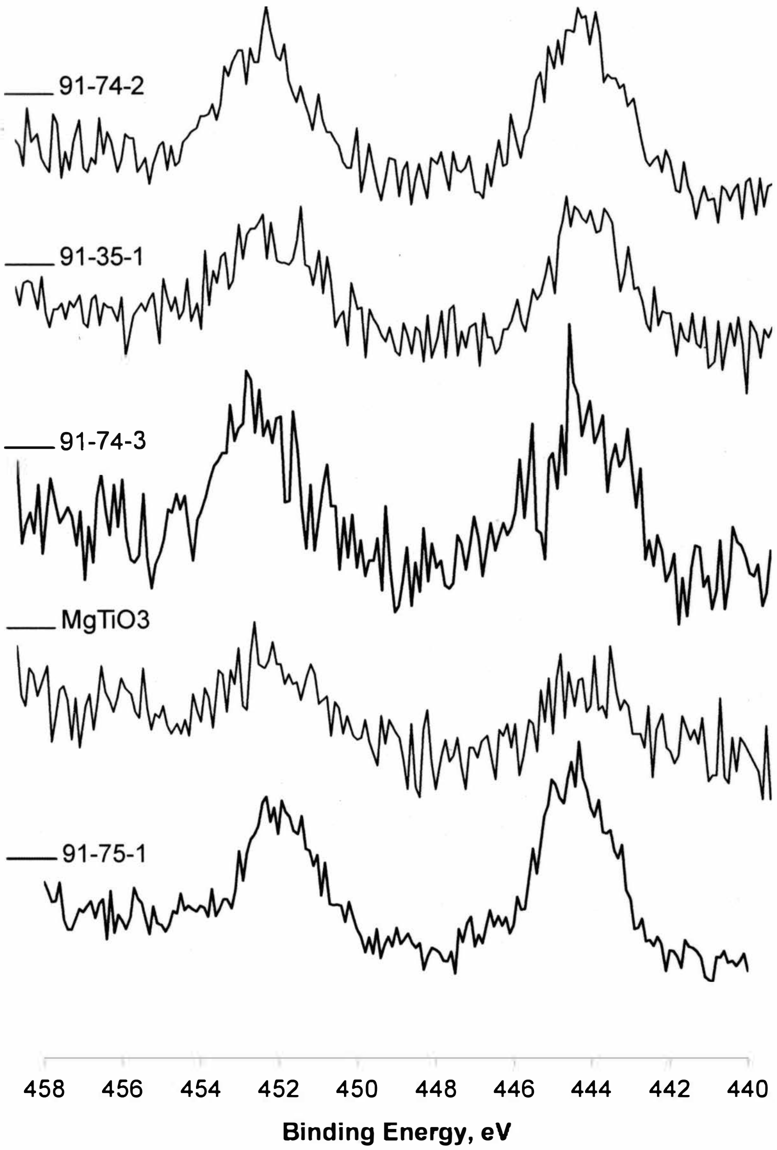

Figure B-1. In $3d_{5/2}$ and $3d_{3/2}$ X-ray Photoelectron Spectra.

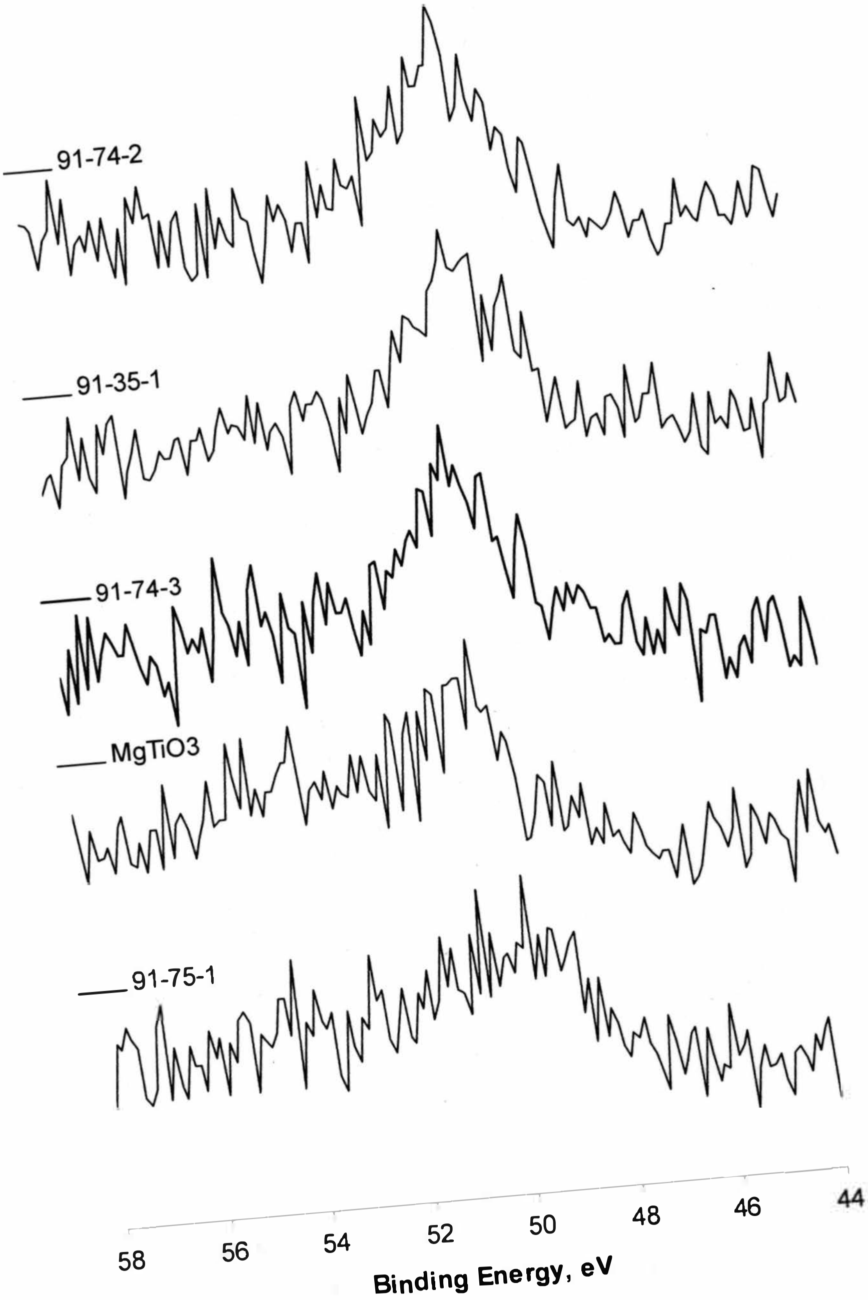

Figure B-2. Mg 2*p* X-ray Photoelectron Spectra.

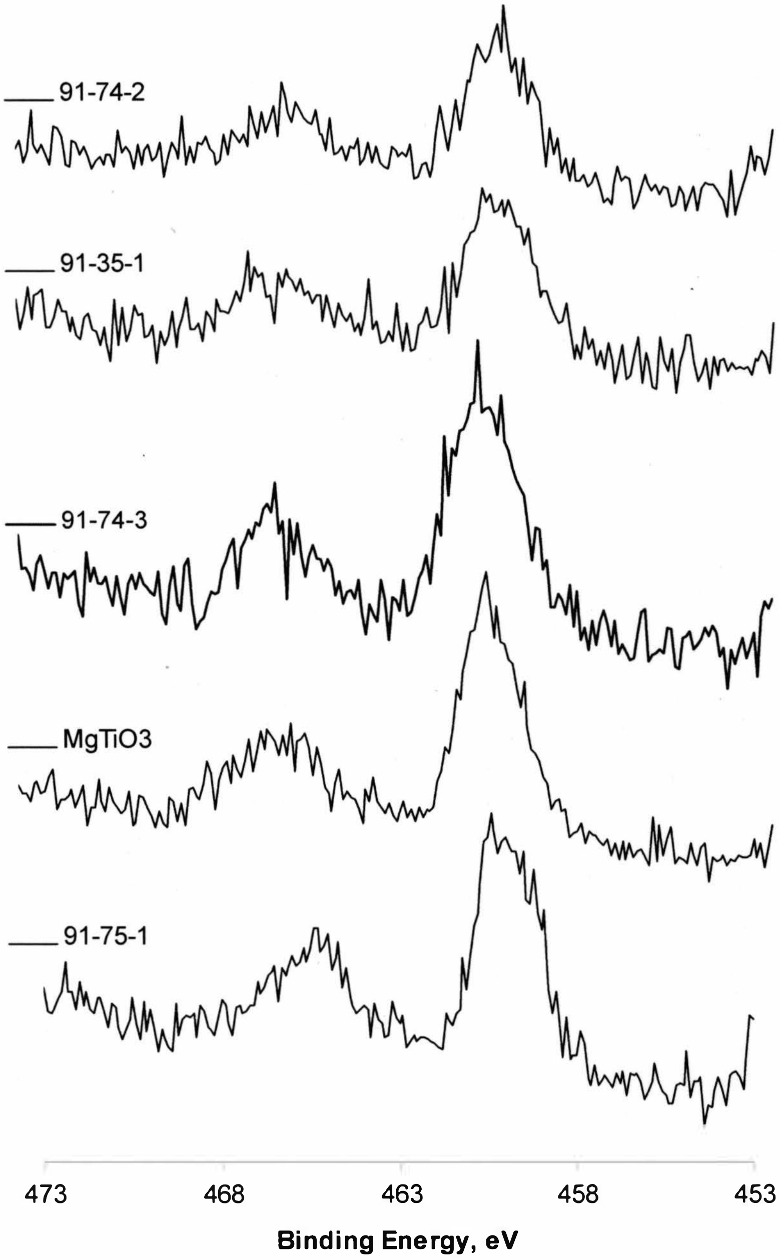

Figure B-3. Ti $2p_{3/2}$ and $2p_{1/2}$ X-ray Photoelectron Spectra.

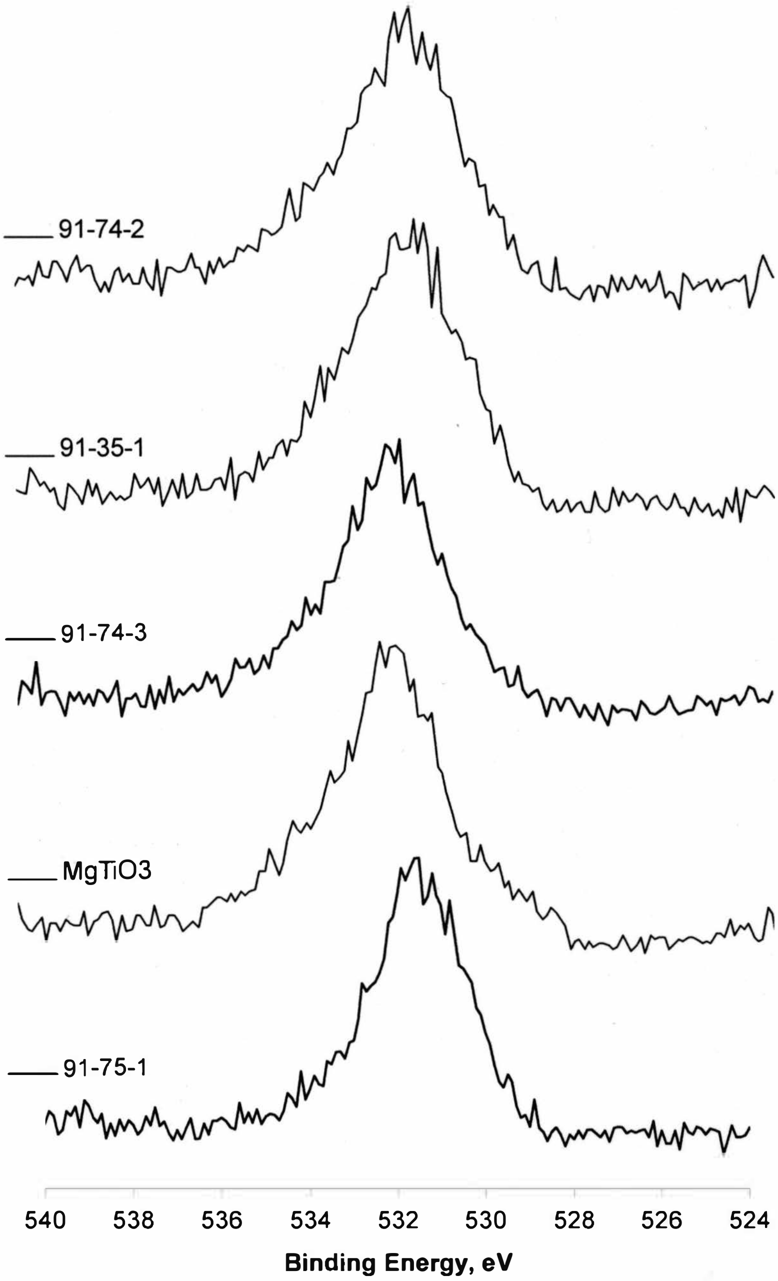

Figure B-4. O 1*s* X-ray Photoelectron Spectra.

BIBLIOGRAPHY

Abothu, I. R., Rao, A. V. P. & Komarneni, S. (1999). *Materials Letters*, 38, 186.

Bacon, G. E. (1962). *Neutron Diffraction*, second edition. London: Oxford University Press.

Bacon, G. E. (1954). *Research*, 7, 257.

Baura-Pena, M. P., Martinez-Lope & Garcia-Claval (1991). *Journal of Materials Science*, 26, 111

Briggs, D. & Seah, M. P. (Ed.) (1994). *Practical Surface Analysis, Volume 1 Auger and X-ray Photoelectron Spectroscopy*, second edition. New York: John Wiley & Sons.

Buras, B. & Holas, A. (1968). *Nukleonida*, 13, 591.

Callister, W. D., Jr. (2000). *Materials Science and Engineering: An Introduction*, fifth edition. New York: John Wiley & Sons.

Cheetham, A. K. & Taylor, J. C. (1978). *Journal of Solid State Chemistry*, 21, 253.

Chiang, Y., Birnie, D. III & Kingery, W. D. (1997). *Physical Ceramics: Principles for Science and Engineering*. New York: John Wiley & Sons.

Cogle, T. J., Mateus, C. A. S., Binks, J. H. & Irvine, J. T. S. (1991). *Journal of Materials Chemistry*, 1, 289.

Cullity, B. D. (1990). *Elements of X-Ray Diffraction*, second edition. Reading, Massachusetts: Addison-Wesley Publishing Company, INC.

Hadjipanyayis, G. C. & Siegel, R. W. (1994). *Nanophase Materials: Synthesis, Properties, and Applications*. Nordrecht, Netherlands: Kluwer.

Jorgensen, J. D., Faber, J. Jr., Carpenter, J. M., Crawford, R. K., Haumann, J. R., Hitterman, R. L., Kleb, R., Ostrowski, G. E., Rotella, F. J. & Worlton, T. G. (1989). *Journal of Applied Crystallography*, 22, 321.

Kimmel, G. & Zabicky, J. (1998). *Materials Science Forum*, 278-281, 624.

Landolt-Bornstein (1959). *Zahlwerte und Funktionen aus der Physik, Chemie, Astronomie und Geophysik*, 6th edition. Berlin: Springler Verlag.

Langford, J. I. & Wilson, A. J. C. (1978). *Journal of Applied Crystallography*, 11, 102.

Larson, A. C. & Von Dreele, R. B. (1985-1994). *General Structure Analysis System.* Universtiy of California.

Liao, J. & Senna, M. (1995). *Materials Research Bulletin*, 30, 385.

McHale, A. E. (1998). *Phase Diagram and Ceramic Processes.* New York: Chapman & Hall.

Moulder, J. F., Stickle, W. F., Sobol, P. E. & Bomben, K. D. (1992). *Handbook of X-ray Photoelectron Spectroscopy*, edited by J. Chastain. Eden Prairie, Minnesota: Perkin-Elmer Corporation.

Pfaff, G. (1994). *Ceramic International*, 20, 111.

Rietveld, H. M. (1969). *Journal of Applied Crystallography*, 2, 65.

Rao, B. K. & Behera S. N. (Ed.) (1998). *Novel Materials Design and Properties.* Commack, New York: Nova Science Publishers, Inc.

Shvets, L. (1980). *Ukr. Khim. Zh.*, 46, 811.

Smyth, J. (2001). http://rugy.colorado.edu/~smyth/min/armalcolite.html.

Steven, A. (1994). *Mechanical Engineering*, 116, 52.

Turberfield, K. C. (1970). *Proceedings of Harwell Summer School on Thermal Neutron Diffraction*, edited by B. T. M. Willis, pp. 34-50. London: Oxford University Press.

Wechsler, B. & Navrotsky, A. (1984). *Journal of Solid State Chemistry*, 55, 165.

Wechsler, B. & Von Dreele, R. B. (1989). *Acta Crystallographica*, B45, 542.

Wormald, J. (1973). *Diffraction Methods*. Oxford: Clarendon Press.

Von Dreele, R. B., Jorgensen, J. D. & Windsor C. G. (1982). *Journal of Applied Crystallography*, 15, 581.

Von Hippel, A. R. (1954). *Dielectrics and Waves*. New York: John Wiley & Sons.

Zabicky, J., Frage, N., Kimmel, G., Hazan, N., El-Fahel, H., Goncharov, E., Manor, E. & Shneck, R. (1997). *Philosophical Magazine* B, 76, 605.

Zabicky, J., Zevin, L., Simon, E., Shneivais, A., Sason, U., Abramovich, L., Ondracek, G., Schuller, M. & Fredel, M. (1993). *Nanostructured Materials*, 3, 77.

Zabicky, J., Zingerman, D., Shneck, R. & Manor, E. (1996). *Nanostructured Materials*, 7, 527.

Zelinski, B. J. J. & Uhlmann, D. R. (1984). *Journal of Physics and Chemistry of Solids*, 45, 1069.